

The Gemini Deep Deep Survey: VIII. When Did Early-type Galaxies Form?

Roberto G. Abraham, Preethi Nair

Department of Astronomy & Astrophysics, University of Toronto, 50 St. George Street, Toronto, ON, M5S 3H4.

Patrick J. McCarthy

Observatories of the Carnegie Institution of Washington, 813 Santa Barbara Street, Pasadena, CA 91101.

Karl Glazebrook[†]

Department of Physics & Astronomy, Johns Hopkins University, 3400 North Charles Street, Baltimore, MD 21218-2686.

Erin Mentuch

Department of Astronomy & Astrophysics, University of Toronto, 50 St. George Street, Toronto, ON, M5S 3H4.

Haojing Yan

Observatories of the Carnegie Institution of Washington, 813 Santa Barbara Street, Pasadena, CA 91101.

Sandra Savaglio

Max-Planck-Institut für extraterrestrische Physik, Garching, Germany

David Crampton, Richard Murowinski

Herzberg Institute of Astrophysics, National Research Council, 5071 West Saanich Road, Victoria, British Columbia, V9E 2E7, Canada.

Stephanie Juneau

Department of Astronomy/Steward Observatory, University of Arizona, 933 N Cherry Ave., Rm. N204, Tucson AZ 85721-0065

Damien Le Borgne[§], R. G. Carlberg

Department of Astronomy & Astrophysics, University of Toronto, 60 St. George Street, Toronto, ON, M5S 3H8.

Inger Jørgensen, Kathy Roth

[†]Present address: Centre for Astrophysics and Supercomputing, Swinburne University of Technology, 1 Alfred St, Hawthorn, Victoria 3122, Australia

[§]Present address: DSM/DAPNIA/Service d'Astrophysique, CEA/SACLAY, 91191 Gif-sur-Yvette Cedex, France

Gemini Observatory, Hilo, HI 96720

Hsiao-Wen Chen[†]

Center for Space Research, Massachusetts Institute of Technology, Cambridge, MA 02139-4307

Ronald O. Marzke

Dept. of Physics and Astronomy, San Francisco State University, 1600 Holloway Avenue, San Francisco, CA 94132

ABSTRACT

We have used the Hubble Space Telescope's Advanced Camera for Surveys (Ford et al. 2003) to measure the cumulative mass density in morphologically-selected early-type galaxies over the redshift range $0.8 < z < 1.7$. Our imaging data set covers four well-separated sight-lines, and is roughly intermediate (in terms of both depth and area) between the GOODS/GEMS imaging data, and the images obtained in the Hubble Deep Field campaigns. Our images contain 144 galaxies with ultra-deep spectroscopy obtained as part of the Gemini Deep Deep Survey. These images have been analyzed using a new purpose-written morphological analysis code which improves the reliability of morphological classifications by adopting a 'quasi-Petrosian' image thresholding technique. We find that at $z \sim 1$ about 80% of the stars living in the most massive galaxies reside in early-type systems. This fraction is similar to that seen in the local Universe. However, we detect very rapid evolution in this fraction over the range $0.8 < z < 1.7$, suggesting that over this redshift range the strong morphology-mass relationship seen in the nearby Universe is beginning to fall into place. By comparing our images to published spectroscopic classifications, we show that little ambiguity exists in connecting spectral classes to morphological classes for spectroscopically quiescent systems. However, the mass density function of early-type galaxies is evolving more rapidly than that of spectroscopically quiescent systems, which we take as further evidence that we are witnessing the formation of massive early-type galaxies over the $0.8 < z < 1.7$ redshift range.

Subject headings: galaxies: evolution

1. INTRODUCTION

The study of galaxy formation and evolution is one of the most active interfaces between observation and theory in contemporary astrophysics. Sophisticated numerical simulations have elucidated the key role of dark matter in driving the formation of structure (e.g. Springel et al. 2005), while the most recent generation of simulations incorporate gas dynamics and highlight the role of feedback (e.g. Croton et al. 2006; Governato et al. 2006). A number of recent galaxy surveys allow one to trace the evolution of stellar systems from high redshift to their present-day counterparts (e.g. Wolf et al. 2004; Borch et al. 2006; Fontana et al. 2006; Scoville et al. 2006a). The combination of deep

imaging surveys with the Hubble Space Telescope (HST) and ground based spectroscopic surveys play a special role, as they provide both structural information and stellar content for galaxies to early epochs (Brinchmann et al. 1998; Scoville et al. 2006b).

Large area shallow surveys (e.g. SDSS) have provided a detailed census of galaxies in the local volume by luminosity, stellar mass, and stellar content (Kauffmann et al. 2003; Nakamura et al. 2003; Tremonti et al. 2004; Mandelbaum et al. 2006). There is a remarkably strong correlation between the structural properties of galaxies, as quantified by the Hubble type for example, stellar content as revealed by integrated spectra, and stellar mass. Galaxies with stellar masses $> 3 \times 10^{10} M_{\odot}$ have colors and spectra indicative of primarily passive evolution, while lower

[†]Present address: Dept. of Astronomy & Astrophysics, University of Chicago, 5640 S. Ellis Ave, Chicago, IL 60637

mass galaxies have blue colors and spectral features indicative of on-going star formation (Kauffmann et al. 2003). The red sequence galaxies are spheroid dominated, the blue sequence galaxies are primarily disk and irregular systems. Understanding the origin of the tight connection between spectral and morphological classes and their mass dependence is critical to a complete picture of galaxy formation and evolution.

Intermediate depth surveys with HST combined with ground-base spectroscopy have shown that the Hubble sequence is largely in place at $z \sim 1$ (e.g. Lilly et al. 1995; Abraham et al. 1996; Brinchmann et al. 1998; Conselice et al. 2005; Kajisawa & Yamada 2005). At higher redshifts, deep surveys (e.g. GOODS) reveal galaxies with structures that are not easily classified into disks and spheroids (Ravindranath et al. 2006; Lotz et al. 2006; Papovich et al. 2005). This trend is even stronger in small area ultra-deep surveys e.g. the Hubble Deep and Ultra-Deep Fields (Abraham et al. 1996; Yan & Windhorst 2004; Coe et al. 2006), although some large disks were present at $z \sim 2.5$ (Labbé et al. 2003; Stockton et al. 2004). Red and Near-IR surveys have shown that the red sequence of massive galaxies was in place at $z \sim 1$, although with number densities lower than today by a factor of $\sim 1.5 - 3$ (Bell et al. 2003; Chen et al. 2002; Faber et al. 2005). Thus it appears that the galaxies acquired their present day morphologies in the $1 < z < 3$ epoch.

The onset of the strong correlation between morphology and stellar content and its dependence on mass is not as well constrained. One of the primary goals of the Gemini Deep Deep Survey (GDDS; Abraham et al. 2004) was to use stellar-mass-selected samples to probe galaxy evolution in the critical $1 < z < 2$ range. The GDDS and other samples (e.g. K20; Fontana et al. 2004) have shown that the total stellar mass density evolves mildly for $z < 1.5$ and that the high-mass end in particular is slowly evolving (Brinchmann & Ellis 2000; Dickinson et al. 2003; Bell et al. 2004; Glazebrook et al. 2004). Many of the most massive galaxies at $z < 2$ have red optical-to-near-IR colors (Glazebrook et al. 2004; Papovich et al. 2006) and spectra dominated by old stellar populations (Cimatti et al. 2004; McCarthy et al. 2004). In this paper we examine the evolution of the stellar mass density as a function of morphological and spectral types using the GDDS spectra and deep HST/ACS imaging. Our analysis is aided by the use of quantitative morphological measurements obtained using a new ‘quasi-

Petrosian’ threshold technique. This allows us to derive robust morphologies over a range of redshifts and apparent magnitudes. We show that the correlation between morphology and spectral class remains strong for passively evolving objects at $z \sim 1.5$ and that the mass densities in spheroids (defined by morphology) and passive systems (defined by stellar content) evolve steeply in the $1 < z < 1.5$ range. These results strongly suggest that the core formation epoch for massive spheroids is drawing to a close in this interval. Signatures of major mergers in the passive population appear to have faded by $z \sim 1.5$ or higher, and subsequent mass evolution at $z < 1$ apparently does not significantly disturb the spectral-morphology correlation. In a subsequent paper we will extend these results to $z \sim 2$ by using NICMOS to explore the rest-frame visible morphologies of the most distant passively evolving galaxies.

We describe our GDDS+HST/ACS sample in Section 2, our approach to quantitative morphological classification in Section 3. Our results are presented in Sections 4 and 5, and discussed in Section 6. Our conclusions are summarized in Section 7. An Appendix at the end of the paper presents a detailed analysis of the robustness of our morphological classification technique. Throughout this paper we adopt a cosmology with $H_0 = 70$ km/s/Mpc, $\Omega_M = 0.3$, and $\Omega_\Lambda = 0.7$. The Vega magnitude system is used throughout.

2. SAMPLE

The GDDS is a spectroscopic survey of an optical and near-IR-selected sample targeting massive galaxies at $0.8 < z < 2.0$. The motivation for the survey, along with selection functions, sampling weights, details of the observations and catalogs, are presented in Paper I (Abraham et al. 2004). Only a brief overview is given here.

The GDDS sample is drawn from four fields in the one square-degree Las Campanas IR imaging survey (McCarthy et al. 2001; Chen et al. 2002), spanning a total area of 121 square arcmin. Broad-band colors were used to pre-select galaxies likely to be in the $0.8 < z < 1.7$ redshift range, and the spectroscopic component of the survey emphasized obtaining high quality spectra for red galaxies at these redshifts. Very long exposures, using the ‘Nod & Shuffle’ technique (Glazebrook & Bland-Hawthorn 2001) to significantly improve subtraction of the night sky emission lines, yielded high quality spectra from which

redshifts could be derived for 308 galaxies to a limit of $I_{\text{Vega}} = 24.5$ mag. The spectra define a one-in-two sparse sample of the reddest and most luminous galaxies near the $I - K$ vs. I color-magnitude track mapped out by passively evolving galaxies in the redshift interval $0.8 < z < 1.7$. This sample is augmented by a one-in-seven sparse sample of the remaining high-redshift galaxy population. The spectra go deep enough to allow redshifts to be obtained for L_{\star} galaxies irrespective of star-formation history at $z \sim 1.5$, and the survey thus targets a mass-limited sample out to this redshift. Because of the importance of cosmic variance, the GDDS fields were carefully chosen to lie in regions of the sky where the number of red galaxies is near the global average (in order to avoid obvious over-densities and obvious voids).

Forty five orbits of imaging observations with the Hubble Space Telescope's Advanced Camera for Surveys were obtained from August 2003 to June 2004. These orbits were distributed over 7 pointings with integration times ranging from 11.7ks to 16.4ks (per pointing). In areas of overlap between pointings (which occur in our SA02 and SA22 fields), the effective integration time can be much larger than this (32.6ks in SA02 and 36.1ks in SA22), albeit over a small area. Our rationale for obtaining relatively long integration times relative to those obtained by surveys such as GOODS (Giavalisco et al. 2004) and GEMS (Rix et al. 2004) will be given in the next section. A tabular summary of our observations is presented in Table 1. ACS images of starforming and post-starburst objects from this sample have already been presented in earlier papers in this series (Savaglio et al. 2005; Le Borgne et al. 2006), while the sample as a whole is examined in the present paper.

Our imaging data cover 67 square arcmin, or 55% of the total area of the GDDS, but by carefully choosing the locations of the pointings within the GDDS fields, and by varying the number of pointings per field, we were able to obtain ACS images for 63% of the galaxies in our spectroscopic sample. Fully reduced ACS F814W images for each of the four fields are shown in Figure 1. Our field orientations were defined to produce additional depth for high priority targets within the allocated orbit total. This resulted in an unusual and non-uniform coverage within each field. The objects within our GDDS+ACS sample are representative of the parent distribution in their local densities and distribution on the sky. Our sub-sample of GDDS galaxies imaged with ACS are neither drawn

from unusually dense regions nor from low density voids.

Using the methodology described in the next section, reliable morphologies can be obtained for galaxies down to $I_{F814W} = 24.0$ mag. Our images contain 3596 galaxies in the LCIRS parent sample, 1519 of which are brighter than our morphological analysis limit. Of these, 144 galaxies are in the GDDS. A detailed breakdown of the numbers of objects in individual fields is given in Table 2.

3. METHODOLOGY

The approach to quantitative morphological classification adopted in the present paper is based on an updated version of the now fairly well-established technique of subdividing the galaxy population into classes on the basis of position on an asymmetry vs. concentration diagram. This approach was first used in Abraham et al. (1996) to analyze the Hubble Deep Field, and variations of it have now been widely adopted (Brinchmann et al. 1998; Conselice 2003; Lotz et al. 2004; Scarlata et al. 2006; Lisker et al. 2006). While details of implementation differ amongst authors, the general approach has been shown to work well for subdivision into broad classifications (e.g. early-types vs. spirals vs. peculiars/mergers). Unfortunately the more subtle distinctions between the morphological classes (e.g. elliptical galaxies vs. S0 galaxies) are not captured by the system.

Our analysis in this paper is based on a new publicly-available code, MOPHEUS, which produces a large number of measurements which can be used to constrain the morphological properties of galaxies in addition to concentration and asymmetry¹. The optimal set of parameters for characterizing galaxy morphology will be explored in Nair et al. 2007 (in preparation), but as will be shown below, for the simple purpose of isolating early-type galaxies from all other galaxy types, a straight-forward diagram based on only two parameters, namely the Gini coefficient and asymmetry, works rather well. The Gini coef-

¹MOPHEUS can be downloaded from the following web site: <http://odysseus.astro.utoronto.ca/~abraham/Morpheus>. Please note that the code base is evolving and the version used in the present paper is the July 2006 release. In addition to incorporating some relatively new parameters (e.g. the Gini coefficient from Abraham et al. 2003 and M20 from Lotz et al. 2004) MOPHEUS also incorporates improvements suggested by others for ways to better measure well-established parameters such as asymmetry (e.g. Conselice et al. 2003).

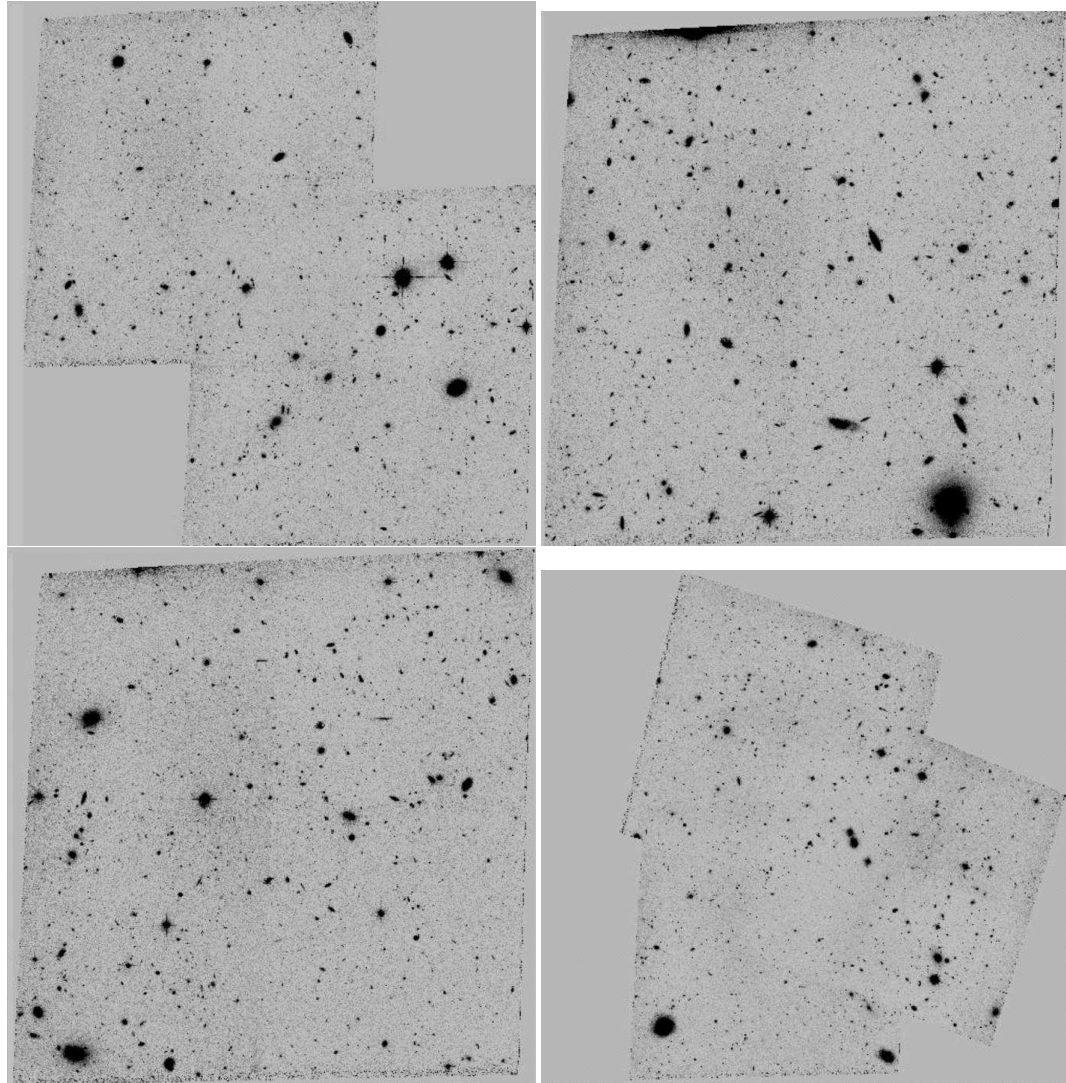


Fig. 1.— Hubble Space Telescope Advanced Camera for Surveys images showing our SA02 field (top left), SA12 field (top right), SA15 field (bottom left) and SA22 field (bottom right). As described in the text, the tiling of the field pointings were chosen to maximize the integration time on galaxies with known high redshifts. Details are given in Table 1.

TABLE 1
LOG OF OBSERVATIONS

Pointing	RA (J2000)	Dec (J2000)	# Visits	# Orbits	Integration time (s)
<i>SA02 (2 pointings, 14 orbits, 32676s total integration time, 19.9 arcmin² area)</i>					
1	02:09:43.48	-04:36:42.0	3	7	16338
2	02:09:37.43	-04:38:34.6	3	7	16338
<i>SA12 (1 pointing, 6 orbits, 14640s total integration time, 11.5 arcmin² area)</i>					
1	12:05:26.71	-07:23:34.2	2	6	14640
<i>SA15 (1 pointing, 5 orbits, 12200s total integration time, 11.4 arcmin² area)</i>					
1	15:23:50.38	-00:04:34.3	2	5	12200
<i>SA22 (3 pointings, 5 orbits, 36070s total integration time, 24.0 arcmin² area)</i>					
1	22:17:38.15	+00:16:35.1	2	5	11670
2	22:17:37.71	+00:14:21.6	2	5	12200
3	22:17:45.09	+00:15:33.2	2	5	12200

TABLE 2
SUMMARY OF THE ACS IMAGING SAMPLE

Sample	SA02	SA12	SA15	SA22	All
Galaxies in the LCIRS parent sample	998	839	748	1011	3596
LCIRS galaxies with $18 < I < 24.0$ mag	375	287	315	542	1519
Galaxies in the GDDS sample	48	29	26	90	193
GDDS galaxies with $18 < I < 24.0$ mag	39	24	11	70	144

ficient is fairly new to astronomy (being introduced in Abraham et al. (2003) and improved in Lotz et al. (2004)), but it has been used in econometrics for nearly a century to quantify the inequality of wealth distributions in human populations (Gini 1912). When applied to galaxy images, the Gini coefficient provides a quantitative measure of the inequality with which a galaxy's light is distributed amongst its constituent pixels, and it can be used as a sort of generalized concentration index that does not depend on galaxy symmetry. Furthermore, as shown in Appendix A, the Gini coefficient remains a surprisingly robust statistic even in the face of morphological K -corrections. We therefore consider classification based on position in the Asymmetry-Gini diagram (referred to as the A-G diagram, or A-G plane) to be an updated and improved version of classification on the basis of the Asymmetry-Concentration diagram (Abraham et al. 1996). The A-G plane will be the central diagnostic diagram in the present paper for purposes of morphological classification.

As noted earlier, Lotz et al. (2004) presented a valuable refinement of the original definition of the Gini coefficient given in Abraham et al. (2003). Lotz et al. (2004) computed the Gini coefficient using circular apertures scaled to multiples of the Petrosian radius. In Section 3.2 below we will show how this idea can be extended using so-called 'quasi-Petrosian' isophotes, which retain all improvements to the Gini coefficient presented by Lotz et al. (2004), and improve the statistic further so it works better for galaxies of arbitrary shape. But before describing our improved statistic, we will describe the importance of having data deep enough to be worth analyzing with these improved tools. Further discussion can be found in Appendix A.

3.1. Required depth

The long integration times obtained in our ACS fields were motivated by our need for reliable morphological classification of early-type galaxies out to $z \sim 2$. Morphological K -corrections impact early-type galaxies in a qualitatively different manner from how they impact late-type galaxies (see Abraham et al. (1996) and Brinchmann et al. (1998) for a more detailed discussion). Late-type galaxies are dominated by irregular knots of star-formation which become more prominent as the observed wavelength probes further to the blue, typically leading to increased asymmetry. On the other hand, early-type galaxies are (by definition) smooth and rather symmetric, and the

changes that occur are more uniform — the central parts of the galaxy remain brightest at all redshifts, and the asymmetry remains low. As is shown in greater detail in Appendix A, morphological classification of early-types from a single band of observation is possible out to high-redshifts, provided the data go deep enough to probe the galaxies out to similar physical radii over the redshift range of interest. Obtaining data of sufficient depth is the crucial ingredient — probably the greatest source of confusion in morphologically classifying early-type galaxies at high redshifts is systematic misclassification of early-intermediate spirals as E/S0 systems, because at high-redshifts $(1+z)^4$ flux diminution lowers the surface brightness of disks below the threshold of visibility, thus increasing the prominence of the central bulge. Our ACS integration times were chosen to be deep enough to avoid this effect.

Figure 2 shows the signal-to-noise/pixel as a function of age and redshift for HST ACS observations of a projected stellar mass density corresponding to that of the Milky Way at the solar radius. The panel on the left corresponds to an exposure time of 3ks, and the panel on the right corresponds to a 20ks integration. Different lines correspond to observations of galaxies at $z = 0.7, 1.2$, and 1.7 (the range of redshifts explored in the present paper). The logarithm of signal-to-noise/pixel is shown as a function of the age of the stellar population, assuming the fairly typical stellar population model described in the caption. To account (rather crudely) for the light smoothing and connected-component optimizations done by the pre-processing imaging segmentation software used (discussed further below), we assume an effective pixel scale of 0.1 arcsec/pixel, and that a SNR/pixel greater than 0.5 is detectable². On this basis, Figure 2 shows that at $z \sim 0.7$ one is able to probe out to large radii in the rest-frame of galaxies even with relatively shallow (e.g. 1 orbit, or 3ks) optical observations obtained with HST. At this redshift, projected mass densities corresponding to the intermediate regions of large disk galaxies are observable for around 60% of the maximum possible age for the galaxy (defined as the age of the Universe at the epoch of observation). However,

²This number is somewhat arbitrary, because in reality the limiting isophotal signal-to-noise is dependant on the smoothing parameter and connected-component algorithm (i.e. 4-point vs. 8-point connectivity) adopted by the segmentation software used to separate out a galaxy's pixels from the underlying sky. A value around 0.5 is reasonable assuming fairly heavy smoothing and 4-point connectivity.

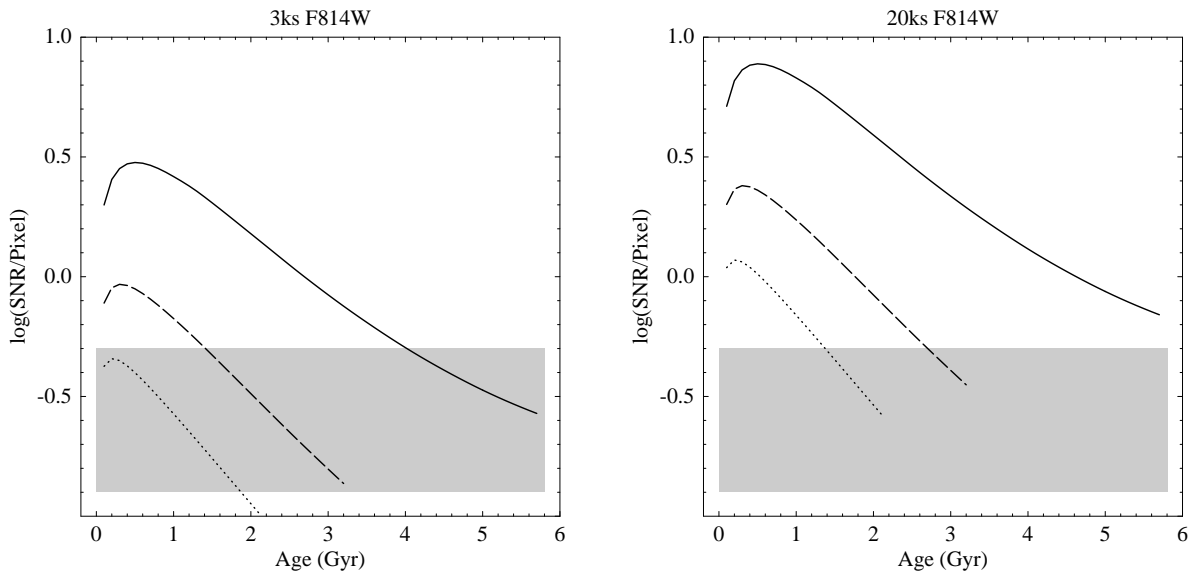


Fig. 2.— Predicted F814W-band $\log_{10}(\text{signal-to-noise/pixel})$ as a function of age for a reference stellar population seen with the HST ACS camera at $z = 0.7$ (solid lines), $z = 1.2$ (dashed lines), and $z = 1.7$ (dotted lines). The panel on the left corresponds to an exposure time of 3ks, and the panel on the right corresponds to a 20ks integration. Calculations are based on a stellar population with a surface stellar mass density of $10^8 M_\odot/\text{kpc}^2$, which is comparable to that of the solar neighborhood. When applying K-corrections we assumed an exponential star-formation history with an e-folding timescale of 1 Gyr, a Miller-Scalo IMF, and 30% solar metallicity. To approximately account for the light smoothing and connected-component optimizations done by SExtractor when segmenting galaxy pixels from the background sky, we assumed an effective pixel scale of 0.1 arcsec/pixel, and that a SNR/pixel greater than 0.5 is detectable. (Note that $\log_{10}(0.5) = -0.301$). With these assumptions, the grey regions shown in the plot are unobservable due to low signal-to-noise. Another factor impacting the observability of the stellar populations is the age of the Universe, so the curves shown are limited to ages less than that of the Universe at each epoch of observation. See text for details.

beyond this redshift biases quickly become rather severe — structural information at optical wavelengths comes only from the densest regions in galaxies (such as bulges), or from the youngest parts of galaxies (such as bright star-formation complexes with ages of less 1 Gyr). By $z = 1.7$ it is simply no longer possible to use shallow HST optical data to compare fairly fundamental characteristics, such as the size and morphology of galaxies, with those of local objects. With 20ks integration times, much fairer comparisons can be made — surface mass densities near that of the solar neighborhood with maximal ages can be probed in an unbiased way out to about $z = 1.2$, and at $z = 1.7$ one is able to probe out to radii comparable to those probed by shallow HST imagery at $z = 0.7$. If, as suggested by Bouwens et al. 2005 (see also Iye et al. 2007), significant star-formation activity only begins around $z \sim 6$ (when the Universe is already about 1 Gyr old, so that the maximal age of a stellar population at $z = 1.7$ is 2.8 Gyr instead of the 3.8 Gyr age of the Universe at that redshift), then Figure 2 suggests that one would be able to probe maximally old stellar populations at solar-neighborhood mass densities out the limits of our survey with 20ks integrations. Our goal in defining the rather complicated-looking ACS imaging field geometry shown in Figure 1 was to cover as many GDDS galaxies with known redshifts as possible, subject to the constraint of having at least 12ks of integration everywhere, and up to 33ks of integration in areas where fields overlap. These areas of overlap were chosen to correspond to regions with many high-redshift galaxies.

Having obtained data of the required depth, the next ingredient needed for reliable morphological classification of early-type galaxies is construction of a morphological catalog whose measurements have been synchronized (as closely as possible) to a common physical radius in the rest-frame of each galaxy. Standard tools can take us part of the way to this goal, and the next stage in our analysis was to create a photometric catalog using SExtractor (Bertin & Arnouts 1996), which constructs a photometric catalog by isolating (or ‘segmenting’) galaxies from the background sky on the basis of fairly complicated criteria, based on differential thresholding followed by stages of image splitting based on connected-component analysis. Synchronizing measurements to a common physical rest-frame is done by using the SExtractor catalog and segmentation maps as the input for our own software (MORPHEUS), which measures galaxy struc-

tural parameters contained within a ‘quasi-Petrosian’ isophote, as defined in the next section.

3.2. Definition of the Quasi-Petrosian Isophote

The classic prescription for dealing with limiting isophote mismatches introduced by $(1 + z)^4$ surface brightness diminution of galaxies is to measure galaxy properties within a circular aperture whose size is a multiple of a galaxy’s Petrosian radius (Petrosian 1976). Our more modern formulation of this basic idea is valid for galaxies of arbitrary shape, and is thus more generally useful for analysis of the very diverse population of galaxies seen in deep HST images.

The ‘quasi-Petrosian’ isophote is constructed using an algorithm which works for galaxies of arbitrary shape. All pixels in the galaxy image (defined using the SExtractor segmentation map) are sorted in *decreasing* order of flux to construct an array, f_i , containing the flux in the i^{th} sorted pixel. This array is then summed over to construct a monotonically *increasing* curve of cumulative flux values:

$$\mathcal{F}_i = \sum_{j=1}^i f_j. \quad (1)$$

In analogy with the definition of the Petrosian radius for a circular aperture, we calculate the Petrosian isophote by determining the pixel index i which satisfies the following equation:

$$f_i = \eta \times \left(\frac{\mathcal{F}_i}{i} \right). \quad (2)$$

Note that $\frac{\mathcal{F}_i}{i}$ is the cumulative mean surface brightness in the sorted array. The flux value of the pixel which solves the equation defines the *quasi-Petrosian isophote*. All pixels brighter than f_i are retained, and all pixels fainter than f_i are discarded. The parameter η is fixed for all galaxies in the sample, and experimentation has shown us that $\eta = 0.2$ is a good choice, probing far enough into the outskirts of nearby galaxies to get outside of regions dominated by nuclear bulges, but not so far out that low and high-redshift samples cannot be fairly compared. Because the data are discrete, Equation 2 will rarely be solved exactly, but a perfectly adequate approximation is obtained by simply noting the index of the first zero crossing of $f_i - \eta \times \left(\frac{\mathcal{F}_i}{i} \right)$. A zero crossing is guaranteed to occur at the last pixel index, and when this occurs it indicates that no quasi-Petrosian isophote exists, and the algorithm converges on the standard isophote as the best

approximation to the quasi-Petrosian isophote. We consider this a rather graceful failure mode, and when it occurs, MORPHEUS simply flags this condition and proceeds with its analysis using the standard isophote.

It is interesting to compare Equation 2 with the definition of the Petrosian radius adopted by the SDSS collaboration (Blanton et al. 2001). In this formulation, one starts with $I(r)$, the azimuthally averaged surface brightness profile of the galaxy. For a given profile, the Petrosian radius, r_p , is the radius r at which the following relation holds:

$$\frac{\int_{0.8r}^{1.25r} dr' 2\pi r' I(r') / [\pi(1.25^2 - 0.8^2)r^2]}{\int_0^r dr' 2\pi r' I(r') / (\pi r^2)} = 0.2. \quad (3)$$

Thus the Petrosian radius is simply the radius at which the local surface brightness in a circular annulus is equal to 20% of the mean surface brightness within the annulus. Understanding this, we see that while Equation 2 looks very different from Equation 3, both operate in a similar way. The factor $(\frac{F_i}{i})$ is simply the mean surface brightness of a galaxy's brightest i pixels, so Equation 2 is essentially comparing the surface brightness at a point to a scaled surface brightness interior to an isophote — the key idea in the standard definition of a Petrosian radius. If a galaxy's light distribution is circularly symmetric and monotonically decreasing from a central pixel, then the positions of the brightest i pixels will closely describe the filling-in of a bounding circle, so in this special case the analogy between Equation 2 and the standard Petrosian formalism is nearly exact. However, Equation 2 remains valid for galaxies of arbitrary shape, and is both operationally easier to calculate and more robust than Equation 3.

Figure 3 shows the fraction of each galaxy's pixels above the isophotal threshold defined by solving Equation 2 for $\eta = 0.2$ in our sample. As noted above, data that is too shallow for reliable classification and analysis is flagged by non-convergence of Equation 2. As shown in Figure 3, the fraction of each galaxy's pixels above the isophotal threshold is less than unity for all galaxies in our sample — therefore a quasi-Petrosian isophote exists for *all* galaxies in our sample. This is not the case when our analysis includes galaxies fainter than $I_{F814W} \sim 24$ mag, and the existence of a quasi-Petrosian isophote can be used as a sensible metric for determining how deep morphological measurements should be pushed to when analyzing

ing a given dataset³. It is interesting to consider how a sample defined by quasi-Petrosian area fraction resembles one based on a signal-to-noise threshold⁴, so the signal-to-noise vs. redshift distribution of the massive galaxy sample considered in the present paper is shown in Figure 4. (See below for the precise definition of this sample). As noted on the figure, our massive galaxy sample has a mean signal-to-noise ratio of about 320. The subset of objects with $z > 1.2$ has a mean signal-to-noise ratio of about 220.

Figure 3 also illustrates a drawback of the quasi-Petrosian approach. Because only a fraction of each galaxy's pixels are being used in our morphological computations, some information is being lost, albeit the pixels with the lowest signal-to-noise in each galaxy. The median fraction of pixels lost is $\sim 50\%$ for galaxies at $F814W < 22$ mag, dropping to $< 20\%$ for galaxies at $F814W \sim 24$ mag. Throwing data away is never a happy choice to have to make, but because of $(1+z)^4$ cosmological surface-brightness dimming, it seems essential to do this (in a careful way) if fair comparisons of morphology over a range of redshifts are to be undertaken. Typically, only the high surface-brightness portions of nearer galaxies in a sample would remain visible at the highest redshifts probed by the same sample, so excising the low-surface brightness portions of bright objects is needed to harmonize regions of comparison over a broad range of redshifts.

We conclude this section by noting, in passing, that there is a rather pleasing conceptual connection between our definition of the quasi-Petrosian isophote given above, and the definition of the Gini coefficient given in Abraham et al. (2003). Both statistics are obtained from simple computations on a ranked pixel list.

4. THE MORPHOLOGICAL MIX OF GALAXIES IN THE GDDS FIELDS

Figure 5 shows small ‘postage stamp’ images of each GDDS galaxy, color coded by their spectral type, in the A-G plane. Galaxies with purely passive spec-

³In other words, if the quasi-Petrosian threshold is not being met for an object, then the data is so shallow that only the inner part of the galaxy is being probed. We thank Edward Taylor at Leiden Observatory for pointing out to us that meeting the quasi-Petrosian threshold condition is a convenient way to determine if data is deep enough for reliable morphological work.

⁴There are several different definitions for the signal-to-noise of an image. In the present paper a galaxy's signal-to-noise means the ratio of its background-subtracted flux to the product of the square root of its isophotal area times the standard deviation of the sky noise.

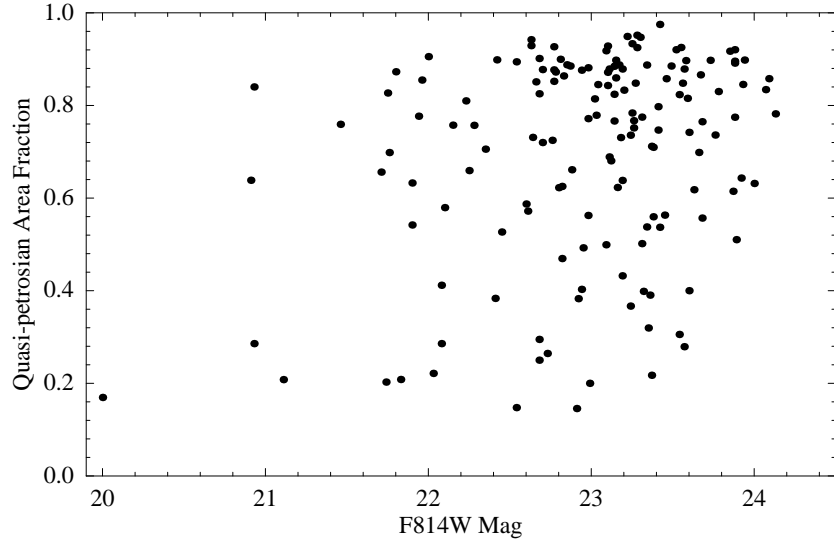


Fig. 3.— The quasi-Petrosian area fraction (the fraction of each galaxy's pixels above the isophotal threshold) plotted as a function I -band magnitude.

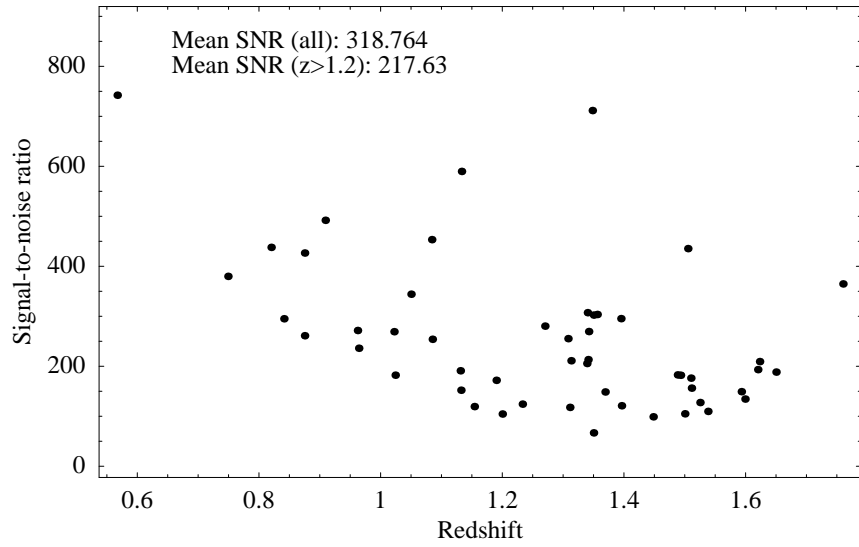


Fig. 4.— Signal-to-noise ratio as a function of redshift for galaxies with stellar masses $\log_{10}(M/M_{\odot}) > 10.5$. These objects constitute our massive galaxy subsample (see text for details). The mean signal-to-noise level of the galaxies shown, and of the subset of objects with $z > 1.2$, are noted near the top of the figure.



Fig. 5.— Asymmetry vs. Gini coefficient for galaxies in the Gemini Deep Deep Survey. The region of this diagram used to isolate early-type systems is marked at the bottom-right corner of the figure. Individual galaxies are shown as 5 arcsec \times 5 arcsec ‘postage stamps’. Circled objects are included in the $\log_{10}(M/M_{\odot}) > 10.5$ massive galaxy subsample defined in the text. The border of each postage stamp is colored according to its spectral classification based on the system described in Paper I. Objects with spectral classifications corresponding to actively star-forming galaxies (classes 100, 110) are shown in blue; quiescent and nearly-quiescent systems (classes 001 and 011) are shown in red; intermediate activity systems (classes 010) are shown in green. Unclassifiable systems with known redshifts are shown with a gray border. (These unclassifiable objects had very limited wavelength coverage because they overlapped with nearby objects on our multi-object spectroscopy masks). Systems with no spectroscopic redshifts are shown without any border. See text for details.

tral types, identified with red borders, have primarily compact early-type morphologies and lie preferentially in the high Gini-low asymmetry region of Figure 5. Galaxies with spectral types characteristic of active star formation have primarily disk and late-type morphologies and occupy a large range of the A-G plane, strongly favoring the high asymmetry and low Gini regions. Galaxies with intermediate or composite spectral types occupy the region of the A-G plane between the passive and star forming galaxies. Figure 5 clearly shows that a strong correlation between morphology, quantified by the A-G plane, and spectral class is in place at the redshifts spanned by the GDDS. For the early-type galaxies in particular, selection by spectral class or morphology are nearly equivalent, and selection by morphology can be undertaken using simple linear cuts in the A-G plane. Throughout the remainder of this paper, we will define early-type galaxies to be those systems with $G > 0.5$ and $A < 0.15$. The choice of $G > 0.5$ is important, and its rationale is discussed in greater detail in Appendix A. The choice of $A < 0.15$ is based simply on visual inspection of Figure 5, but is not particularly fundamental for the limited purposes to which we are presently applying this diagram (namely, for determining the cumulative mass function of massive early-type galaxies). This can be seen directly from Figure 5, where we have drawn circles around those objects which meet the mass completeness cut used when determining our mass functions (to be described in the next section). In fact, so few high mass systems lie above the asymmetry cut that our main conclusions do not change if no asymmetry cut is imposed at all. Therefore, our classification system for massive early-type galaxies is fundamentally based on the Gini coefficient.

The concordance between morphology and spectral type is shown more clearly in Figure 6, where we present the individual images of galaxies classed as being early-type using our formalism. Visual inspection of this figure is consistent with all galaxies being early-type systems. Approximately 15% (5/30) of the galaxies do show weak disks, but without spiral structure, and these are probably S0 or S0/a systems. Clearly the A-G diagram does not discriminate between E and S0 galaxies.

5. THE EVOLVING MASS-DENSITY FUNCTION OF MASSIVE EARLY-TYPE GALAXIES

In this section we will attempt to synthesize the evolutionary history of massive early-type galaxies by exploring the growth in their cumulative mass density in three broad redshift bins. The mass density functions were computed using the standard V_{max} formalism described in Paper III (Glazebrook et al. 2004), to whom the reader is referred for details. For present purposes it suffices to just highlight a few points that are important to bear in mind when interpreting the models.

It is important to note that our models assume a Baldry & Glazebrook (2003) Initial Mass Function (IMF), which has the same high-mass slope as a Salpeter IMF but which has a break at 1 solar mass (providing more realistic M/L values)⁵. Whenever we compare our results to those in the literature, we always convert to this standard IMF. Typical uncertainties in our model masses are around 0.2 dex in the main $K < 20.6$ sample considered in the present paper.

Because the GDDS is a sparse-sampled survey, each galaxy in the survey acts as a proxy for a number of other objects with similar magnitudes and colors, so determining the stellar mass contributed by an individual galaxy is only the first step in computing the mass function. The volume-weighted contribution of this galaxy to the integrated mass density in a redshift bin is computed using the sampling weights tabulated in Paper I. These weights account for the fact that the GDDS is not completely homogeneous, because when designing spectroscopic masks a higher priority was given to red galaxies than to blue galaxies. The sampling weights quantify the selection probability as a function of $I - K$ and K , with reference to the full wide-area LCIRS tiles which formed the basis for the GDDS sample (and so also account approximately for the effect of cosmic variance).

For maximum robustness in the present paper we focus our analysis on cumulative mass functions for systems above a mass threshold. We adopt a threshold of $\log_{10}(M/M_{\odot}) > 10.5$. As shown in Figure 1 of Paper III, this is the limit to which the GDDS is mass-complete for $z < 1.7$. In other words, red galaxies

⁵The following convenient relationship (accurate to within a few percent independently of the SFH) can be used to convert between mass-to-light ratios measured using our chosen IMF and those determined with a Salpeter IMF: $M/L_K(BG) = 0.55M/L_K(SP)$.

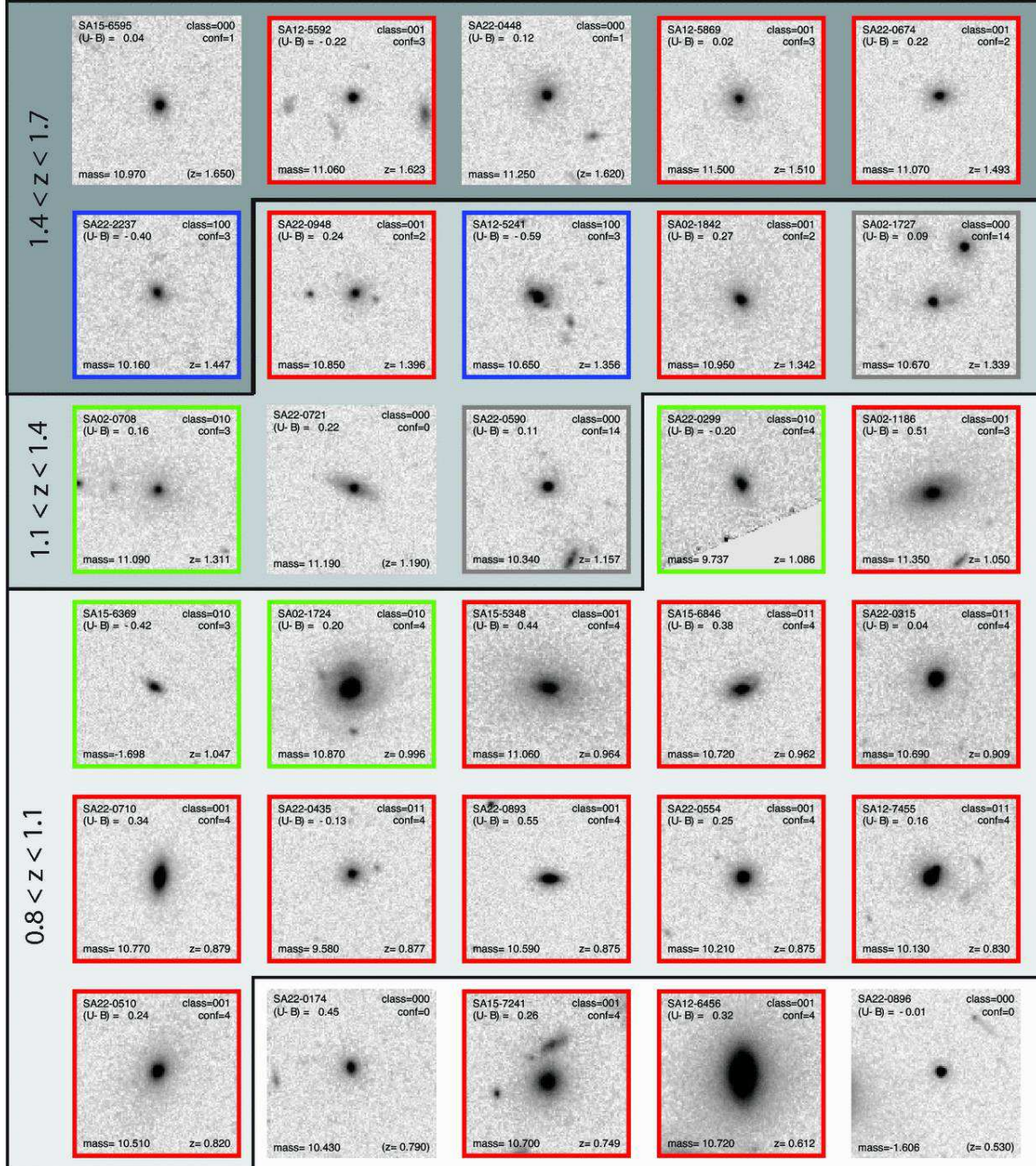


Fig. 6.— Postage-stamp images showing the morphologies of the 30 objects classified as early-type galaxies on the basis of the system described in the text. Galaxies are shown sorted in order of decreasing redshift. Each image is 5 arcsec by 5 arcsec in size, and labeled with the galaxy's ID number, spectroscopic classification, redshift confidence class, rest-frame (U-B) color, redshift, and stellar mass inferred from our best-fit model. Objects without high-confidence spectroscopic redshifts have their redshifts labeled in parentheses. The borders of each image are colored according to spectroscopic classification, as described in the caption to Figure 5. Gray regions surrounding groups of postage stamps indicate which of three broad redshift bins the objects fall within. These bins are used to calculate the cumulative stellar mass function described in §5.

with stellar masses of $\log_{10}(M/M_{\odot}) < 10.5$ would begin to drop out of our survey at the highest redshifts. Another issue that arises when computing the cumulative mass function is the treatment of objects without redshift information. Because the GDDS has a redshift completeness of over 85 percent in the redshift range explored in this paper, the issue is not of overwhelming importance, and none of the conclusions in this paper change if galaxies without redshifts are simply omitted. However, for the sake of consistency we will treat these objects in the same way as they were treated in Paper III. We therefore assign photometric redshifts (computed for the LCIRS by Chen et al. (2002)) to objects without redshifts, and to objects whose redshift confidence class is < 2 . (See Table 3 of Paper I for a detailed description of these confidence classes).

The cumulative mass density function for systems more massive than $\log_{10}(M/M_{\odot}) = 10.5$ is shown in Figure 7. The mass density function shown was computed in three redshift bins ($0.8 < z < 1.1$, $1.1 < z < 1.4$, and $1.4 < z < 1.7$). The corresponding error bars were estimated by a bootstrap analysis. Plot symbols in Figure 7 denote the following subsets of galaxies: (1) Spectroscopically quiescent objects (spectral class 001) shown as diamonds; (2) morphologically selected (on the basis of position in the A-G plane) early-type galaxies shown as circles; and (3) all galaxies shown as squares. At the $z = 0$ position we also plot the corresponding local stellar mass densities, based on the analysis of SDSS observations given by Bell et al. (2003) and converted to our IMF, and incorporating our mass cut. (Note however that the local early-type point is based on color selection, rather than on morphological classification; this point is discussed further below). The cumulative mass functions for all galaxy types from Fontana et al. (2004) and Bundy et al. (2006) are shown in gray.

The most striking aspect of Figure 7 is that the cumulative mass locked up in morphologically-selected early-type galaxies appears to be increasing with cosmic time substantially more quickly than the global rate. The cumulative stellar mass locked up in massive galaxies as a whole is increasing slowly by comparison, changing by only about 0.3 dex over the redshift range probed, in agreement with the trends shown in Paper III. (This is reassuring, because our ACS imaging observations cover only 55% of the area in the complete GDDS). The cumulative stellar mass in spectroscopically quiescent systems is consistent with being flat, although the error bars are large, and we can-

not rule out that the spectroscopically quiescent systems are evolving at a similar rate to that of the total galaxy population.

In our highest redshift bin the fraction of the total stellar mass contained in massive early-type galaxies is similar to that contained by spectroscopically quiescent systems (around 30% of the total). In our lowest redshift bin over twice as much mass is contained in early-type galaxies as is contained in quiescent systems — in fact, early-type systems in our lowest redshift bin contain about 80% of all the stellar mass locked up in galaxies with $\log_{10}(M/M_{\odot}) > 10.5$. This is consistent (within the considerable error bars) to the corresponding value in the local Universe (69%), which can be obtained from Figure 7 by simply dividing the values shown for the two points at $z = 0$. Figure 7 therefore suggests that over the redshift range probed by the GDDS we are witnessing the formation of early-type galaxies as the dominant members of the high-mass end of the galaxy population, the same position they maintain up to the present day. The result from the mass function is in entirely consistent with the visual impression one obtains by simply plotting the morphologies of massive galaxies in our sample as a function of redshift, as shown in Figure 8. The postage stamp images in this figure are shown in order of decreasing redshift, with early-type systems (based on our quantitative definition) circled. The steady increase with cosmic epoch in the fraction of early-type systems as a fraction of the massive galaxy population is rather striking. It seems fairly plausible to conclude that at lowest redshifts probed by the GDDS, early-type galaxies comprise a similar fraction of the massive galaxy population as is seen locally.

6. DISCUSSION

In the local Universe early-type galaxies are nearly always associated with quiescent stellar populations, so the steep evolution of early-types in the cumulative mass function shown in Figure 7 might be viewed as a surprise given the relatively shallow evolution in totally quiescent galaxies. A plausible explanation for this mismatch is offered by the possibility that morphological transformations and stellar mass assembly operate on different time scales. For example, it has long been argued (Baugh et al. 1996; Kauffmann & Charlot 1998; De Lucia et al. 2004) that the bulk of the stars in quiescent early-types galaxies might have formed before these stars were orga-

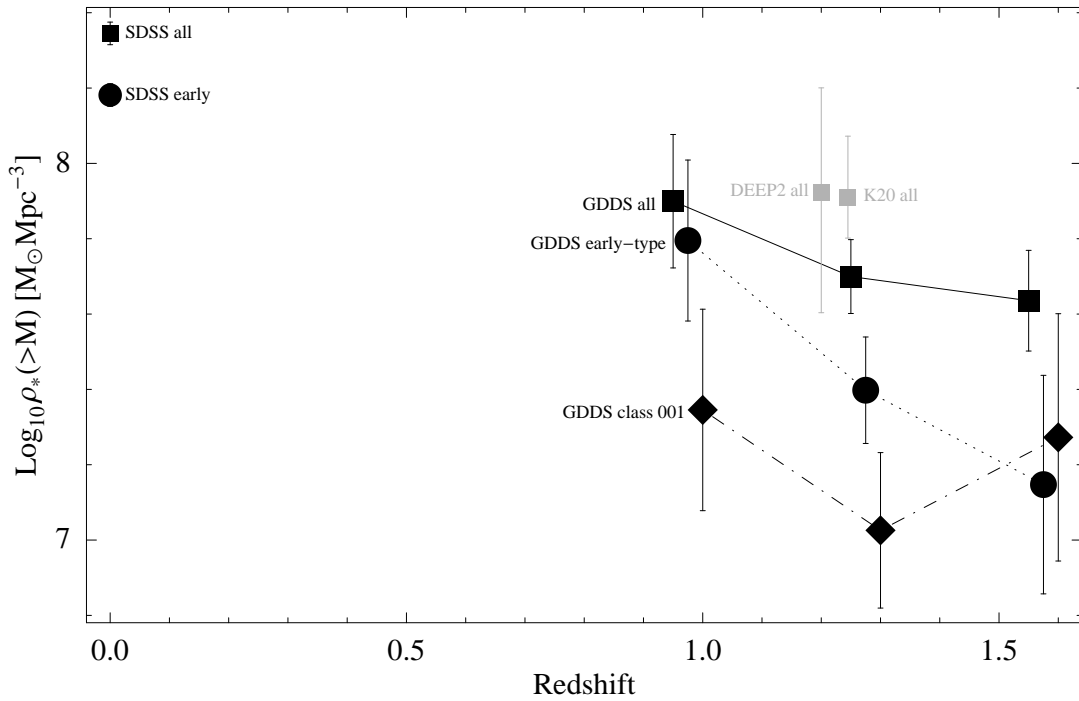


Fig. 7.— Mass density functions for subsets of massive galaxies. As described in the text, our stellar mass cut is set at $\log_{10}(M/M_{\odot}) > 10.5$. Plot symbols denote the following subsets: quiescent (spectral class 001) galaxies [diamonds]; morphologically selected (on the basis of position in the A-G plane) early-type galaxies [circles]; and all galaxies [squares]. The corresponding local stellar mass densities for massive galaxies, taken from the analysis of SDSS observations given by Bell et al. (2003) and converted to our IMF and mass cut, are also shown. The two points shown in light gray are taken from DEEP2 survey work presented by Bundy et al. (2006), and from the K20 analysis published in Fontana et al. (2004)

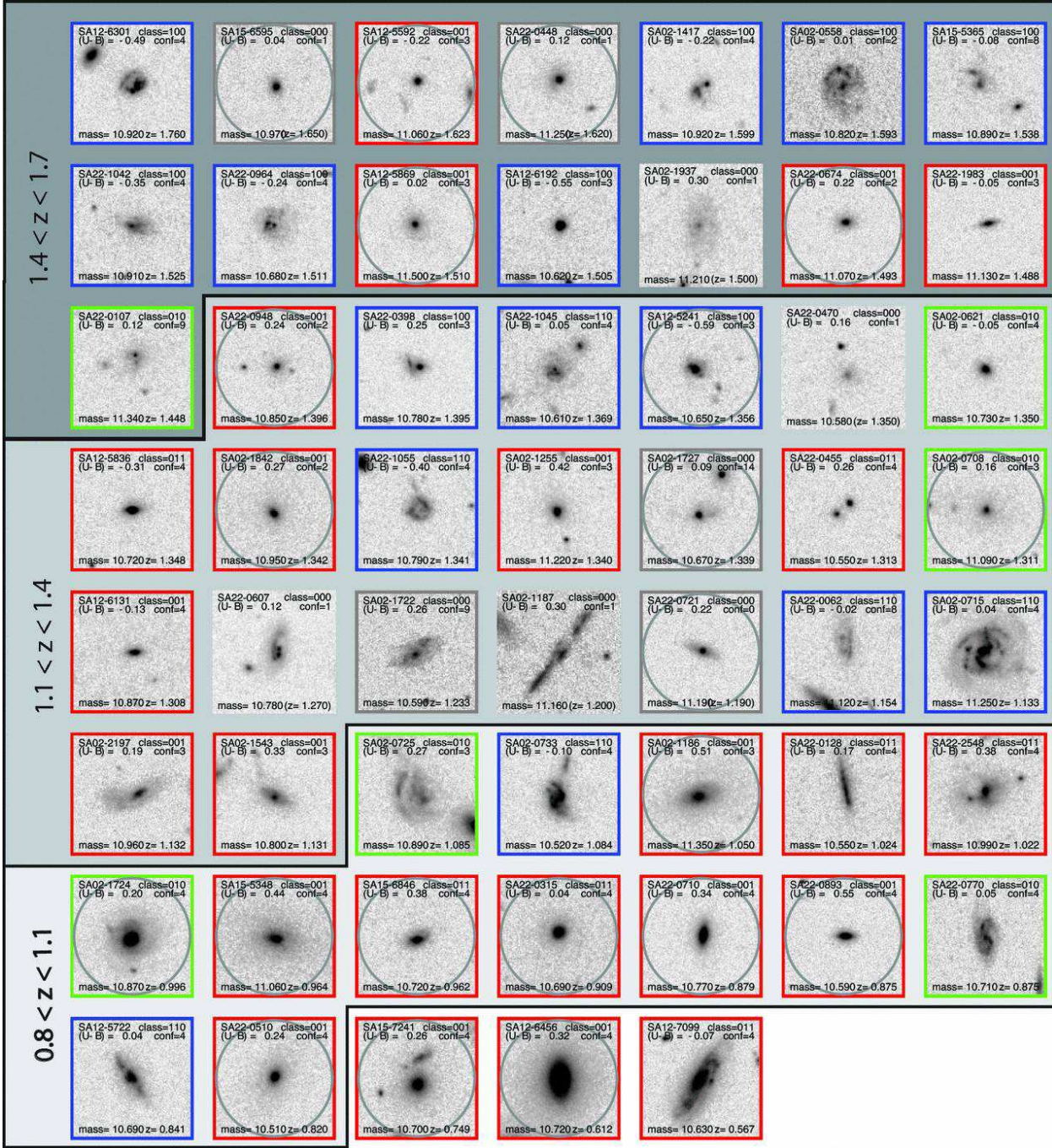


Fig. 8.— Postage-stamp images showing the morphologies of the 54 galaxies in our sample with $\log_{10}(M/M_{\odot}) > 10.5$, sorted in order of decreasing redshift. Early-type galaxies are circled. Each image is 5 arcsec \times 5 arcsec in size, and labeled with the galaxy's ID number, spectroscopic classification, redshift confidence class, rest-frame (U-B) color, redshift, and stellar mass inferred from our best-fit model. Objects without high-confidence spectroscopic redshifts have their redshifts labeled in parentheses. The border of each galaxy image is colored according to the galaxy's spectroscopic classification, as described in the caption to Figure 5. Gray regions surrounding groups of postage stamps indicate which of three broad redshift bins the objects fall within. These bins are used to calculate the cumulative stellar mass function described in the text.

nized into spheroids, in which case the progenitors of such galaxies might be found in other morphological types. On the other hand, it might also be argued that the signatures of star-formation (e.g. blue colors and emission lines) remain in place for a period of time subsequent to the formation of an early-type galaxy, in which case the progenitors of quiescent early-type systems might still resemble early-types, but with blue colors and/or emission lines. We suspect that both scenarios are at play in driving the steep evolution in the cumulative mass function of early-type galaxies shown in Figures 7 and 8.

To further explore the link between morphology and star-formation history, Figure 9 shows the rest-frame ($U - B$) color of our sample, plotted as a function of redshift. The rest-frame colors of our galaxies were computed using the best-fit spectral energy distribution templates used to construct our mass functions. The line shown near the top of the figure is the evolutionary track of an instantaneous starburst forming all of its stars at $z = 3$. Morphologically-classified early-type galaxies are circled. A number of interesting points emerge from this figure. As noted earlier, most morphologically-defined massive early-type galaxies are very red, but the figure shows that a number of massive early-type galaxies with blue colors, probably from young stellar populations (as they do not exhibit AGN features in their spectra). The existence of these objects should come as no surprise, since studies of internal color variations in early type galaxies have shown that a significant fraction of early-type galaxies at $z \sim 1$ have blue cores (Abraham et al. 1999; Menanteau et al. 2004; Papovich et al. 2005). Furthermore, such systems emerge from any scenario in which early-type galaxies are being built up over the redshift range of our survey with minor bursts of star formation occurring in time-scales longer than the stellar relaxation time. It is interesting to note that at high redshifts the red-end of the galaxy distribution lies consistently to the blue of the passive evolution model, and that at low redshifts most blue early-type systems are not very massive — presumably both these effects are manifestations of cosmic downsizing (Cowie et al. 1996; Kodama et al. 2004; Glazebrook et al. 2004; Fontana et al. 2004; Bauer et al. 2005; Juneau et al. 2005; Faber et al. 2005; Bundy et al. 2006). We speculate that most of the ‘blue’ early-type galaxies are ultimately destined to turn into the quiescent early-type galaxies of intermediate mass. We also note that Figures 5 and 8 both show that the abundance of this class

of object would increase significantly if we were less stringent in requiring that early-type galaxies have low asymmetry, since inspection of these figures shows that a number of high Gini systems with high asymmetry have not been included in our sample of early-type galaxies. The asymmetric component of these massive objects is near their nuclei, and we suspect they are late-stage mergers. A number of such systems exhibit quiescent spectra, and these would seem to be good candidates for “dry merging” (van Dokkum 2005), though they may also be systems with high dust contamination. In any case, these objects are heavily outnumbered by star-forming systems. Figure 9 also shows that a sizeable fraction of galaxies with very red rest-frame colors are *not* early-types. These objects comprise only 15% of the red galaxies at $0.7 < z < 1.0$, but contamination rises quickly with redshift, and by $z \sim 1.5$ about half the objects with red rest-frame colors are not early-types. While the existence of these objects is not a surprise — a number of recent papers have shown that color selection used to define early-type galaxy samples results in a mixed bag of galaxies (Yan & Thompson 2003; Moustakas et al. 2004) — the rapid change in the contamination rate as a function redshift is rather striking.

Since color-selected samples cannot be used to define samples of early-type galaxies without significant contamination, it is interesting to consider whether better samples of early-types might be constructed using spectroscopy. Figure 10 shows the F814W images of the 21 galaxies classified as purely quiescent (class ‘001’ in the taxonomy of Paper I) in our ACS sample. About 2/3 of the sample (13/21) are early-types using our automated classifier. About half the remainder are objects that would be classified as early-types if our asymmetry cut were slightly less rigorous, and on the whole the sample appears fairly homogeneous. We conclude that a fairly good sample of early-type galaxies could be defined simply by selecting purely quiescent systems. However, Figure 11 makes it clear that care would have to be taken to exclude objects showing even small amounts of star-formation. This figure shows a montage of the 12 galaxies in our imaging sample with spectral classifications corresponding to a dominant old stellar population contaminated by low-level star formation (class ‘011’ in the taxonomy of Paper I). It is obvious that these objects have a wider range of morphologies than those with the ‘001’ (quiescent) spectral class and a higher fraction of disks, and 2/3 of these objects lie outside the region in the

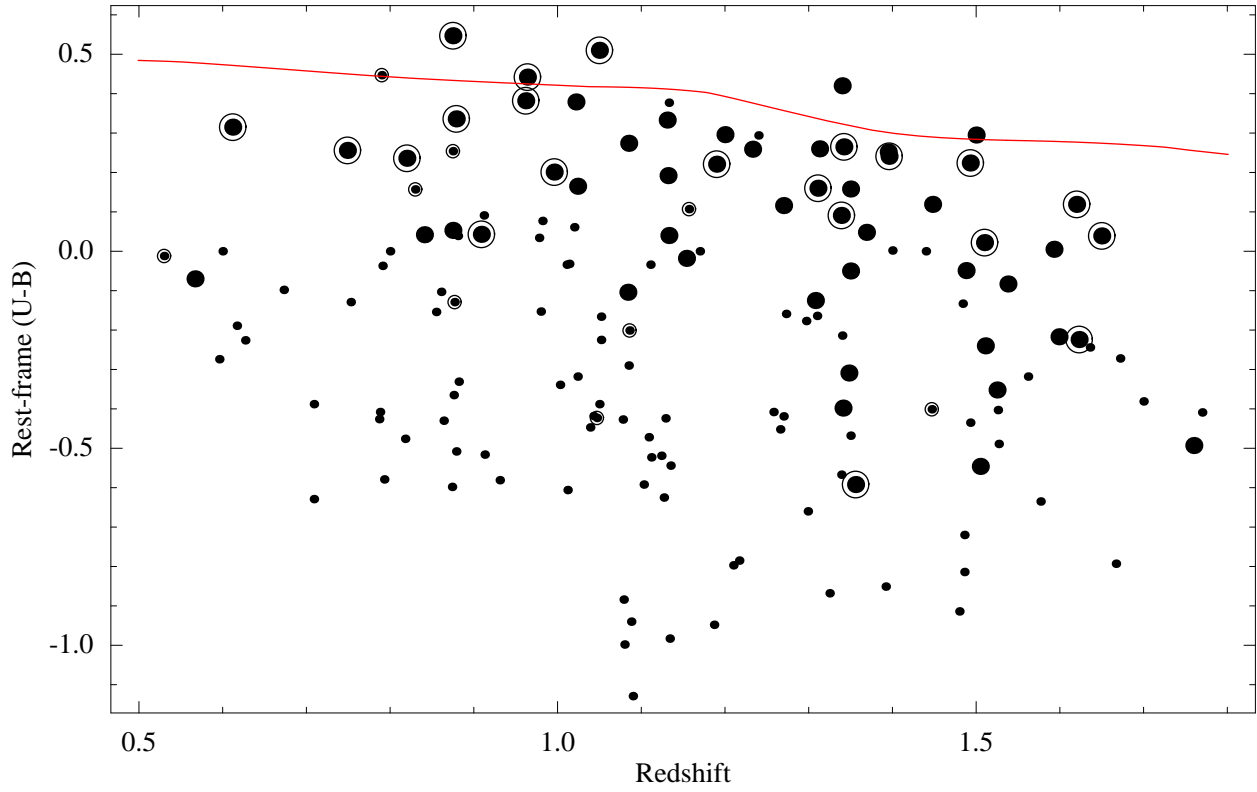


Fig. 9.— Rest-frame $(U - B)$ color of our sample, plotted as a function of redshift. Galaxies with $\log_{10}(M/M_{\odot}) > 10.5$ are shown with large symbols. Morphologically classified early-type galaxies are circled. A fraction of the other red galaxies are massive and highly-reddened star-forming galaxies (Noll et al. 2006). The line shown near the top of the figure is the evolutionary track of a massive instantaneous starburst forming all of its stars at $z = 3$. See text for details.

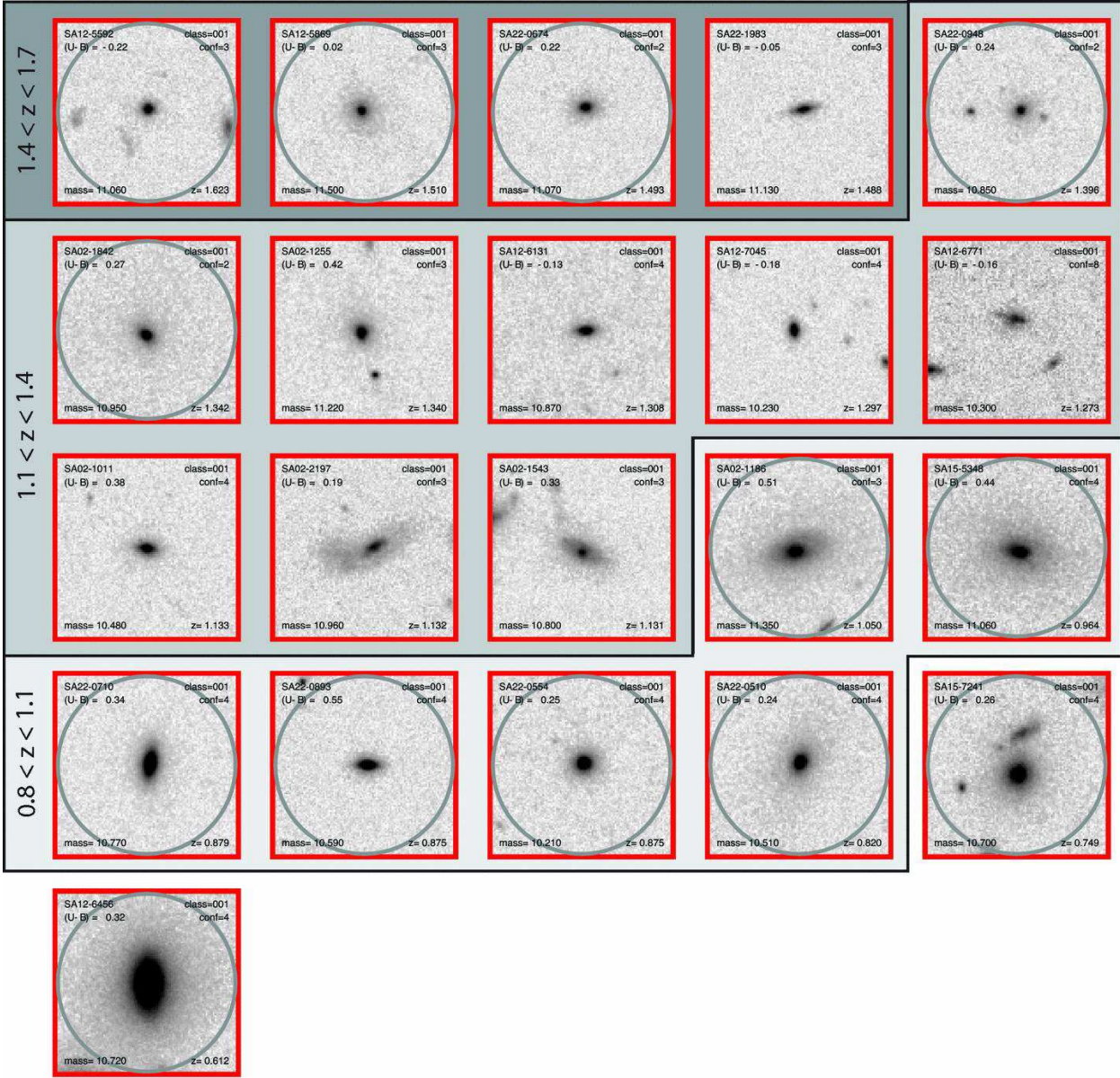


Fig. 10.— 5 arcsec by 5 arcsec images of the 21 galaxies in our ACS imaging sample with spectral classifications corresponding to quiescent stellar populations (class 001). Early-type galaxies are circled. Gray regions surrounding groups of postage stamps indicate which of three broad redshift bins the objects fall within. These bins are used to calculate a cumulative mass function, as described in §5. See text for details.

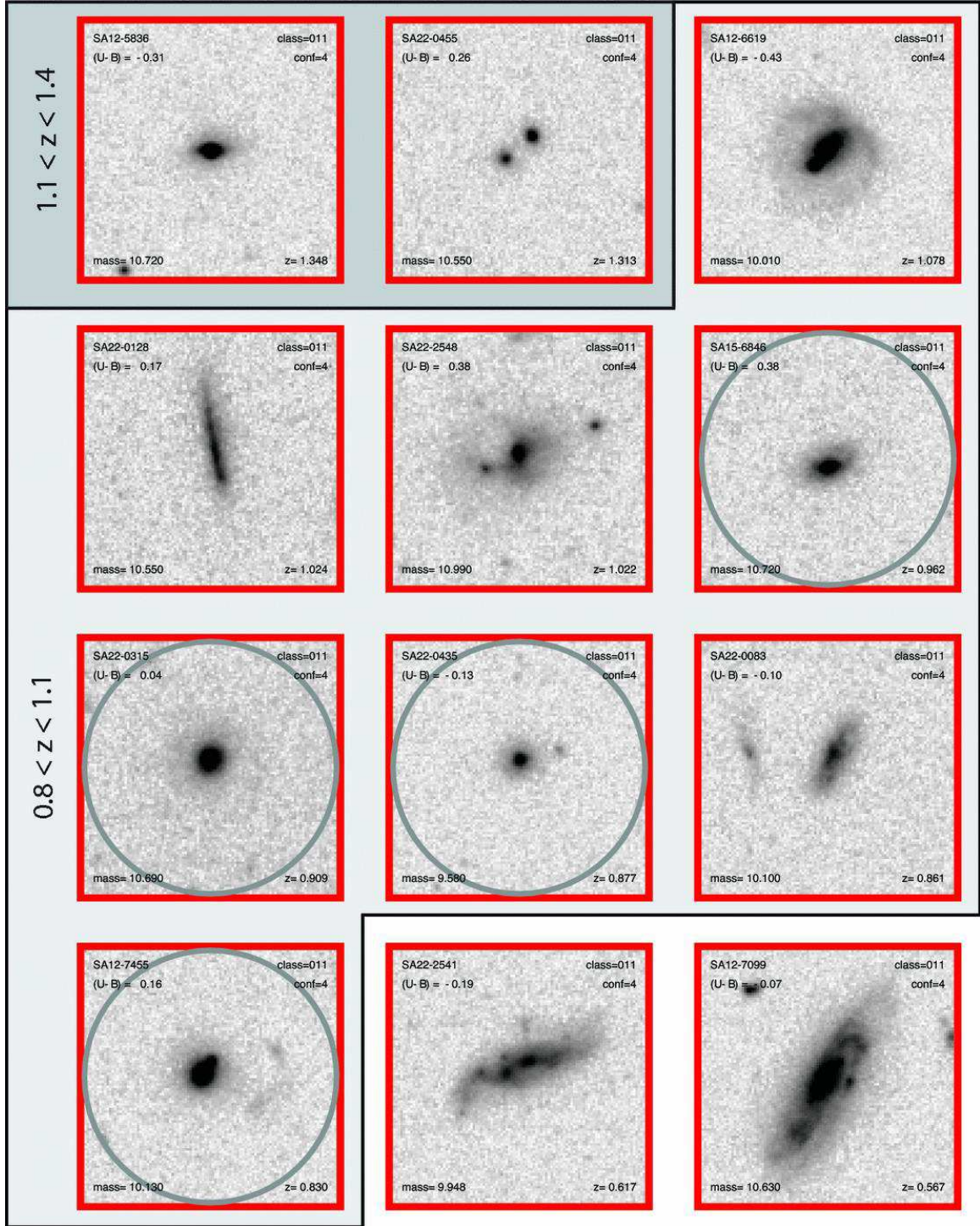


Fig. 11.— 5 arcsec by 5 arcsec images showing the morphologies of the 12 galaxies in our imaging sample with spectral classifications corresponding to a dominant old stellar population augmented by low-level star formation (class 011). Early-type galaxies are circled. Gray regions surrounding groups of postage stamps indicate which of three broad redshift bins the objects fall within. These bins are used to calculate a cumulative mass function, as described in §5.

A-G plane used to isolate early-type systems. Approximately 50% of the old + weak/truncated star formation objects are disks and many show prominent HII regions. The remaining objects are compact and have early-type morphologies. We can only speculate on the ultimate destiny of the large disk galaxies in this sample. Several of these objects have prominent bulges, and fading of their disks might bring them rather close to meeting our criterial for early-type galaxies. It is tempting to identify these with fairly recent merger events that will relax to the passive and early-type systems at $z < 1$. Indeed these objects are closely related to the massive post-starburst systems described in Le Borgne et al. (2006) (Paper VI). They appear to have undergone significant star formation episodes at $z \geq 1.5$ and, barring further star burst episodes, will appear as passive systems on the red sequence by $z \sim 0.8 - 1$. (We note that spectroscopy of color-selected samples – Yan & Thompson (2003) – have also revealed luminous disk galaxies with red colors and spectra dominated by old stars.)

Our results paint a picture of the *morphological assembly* of many massive early-type galaxies over the redshift range $1 < z < 2$, but it is important not to take this conclusion too far. Large area surveys (Brown et al. 2006) clearly indicate that the most massive systems have formation redshifts, both stellar and dynamical, well above the redshift limit of our present sample. The age analysis carried out in Paper IV and similar analyses of other samples (e.g. Cimatti et al. 2004; Heavens et al. 2004; Jimenez et al. 2006) suggest that these objects formed at $z > 3$ on average and in some cases at considerably higher redshifts. As we will show in a subsequent paper, the rest-frame R-band morphologies of the passive galaxies with $z > 1.3$ are consistent with early dynamical formation as well. These results are another manifestation of the popular down-sizing paradigm in which massive galaxies form early and less massive systems are assembled at later times (Cowie et al. 1996; Juneau et al. 2005). At the low-redshift end of our sample, the convergence in the fractional mass density in massive early-type galaxies (relative to the total mass density at the same redshift) to something similar to the value in the SDSS indicates that the epoch of massive early-type formation may be drawing to a close by $z \sim 1$ (a conclusion consistent with the high post-starburst fraction described in Paper VI).

The offset in the mass density contained in the lowest redshift GDDS point in Figure 7 and the local data

point is rather striking, and this *may* indicate that whatever process is driving the process of massive galaxy assembly at $z < 1$ is operating in a way which conserves the overall fraction of early-types even as it builds the total stellar mass in the galaxy population from $z = 0.7$ to $z = 0$. However, we remain a little skeptical about this conclusion. The most robust statements that can be made from Figure 7 are based on *relative measurements internal to each dataset*. Comparing the high-redshift GDDS points to their low-redshift counterparts in Figure 7 is dangerous, even though we chosen to plot them together in the same diagram. Bell et al. (2003) note that there is an at least $\sim 30\%$ systematic uncertainty in the local estimate, and the uncertainty in the high-redshift points is likely to be at least this big. Another source of potential bias is that Bell et al. (2003) define their early-type sample on the basis of color, rather than on the basis of morphology. Much of the offset between the cumulative stellar mass locked in early type at $z = 0$ and $z > 0.7$ may be due to systematic differences in the way samples of high-redshift and low-redshift early-type galaxies are constructed — once again, we emphasize that the trends seen internally to either data set are more reliable.

7. CONCLUSION

We have described an improved methodology for morphologically classifying galaxies, based on ‘quasi-Petrosian’ image segmentation. This results in more robust measurements of galaxy properties at high redshifts. This methodology has been applied to define a sample of early-type galaxies in HST ACS images of the Gemini Deep Deep Survey fields. Using this sample, we computed the cumulative stellar mass functions of morphologically-segregated subsets of galaxies with $\log_{10}(M/M_{\odot}) > 10.5$. Although our error bars are large, we find striking evidence for evolution in the fraction of stellar mass locked up in massive early-type galaxies over the redshift range $0.7 < z < 1.7$. This redshift range corresponds to that over which massive early-type galaxies morphologically assemble, and over which the strong color-morphology correlations seen in the local Universe begin to fall into place.

Acknowledgments

This paper is based on observations obtained at the Gemini Observatory, which is operated by the Association of Universities for Research in Astronomy,

Inc., under a cooperative agreement with the NSF on behalf of the Gemini partnership: the National Science Foundation (United States), the Particle Physics and Astronomy Research Council (United Kingdom), the National Research Council (Canada), CONICYT (Chile), the Australian Research Council (Australia), CNPq (Brazil) and CONICET (Argentina).

Based on observations made with the NASA/ESA Hubble Space Telescope, obtained at the Space Telescope Science Institute, which is operated by the Association of Universities for Research in Astronomy, Inc., under NASA contract NAS 5-26555. These observations are associated with program #9760. Support for program #9760 was provided by NASA through a grant from the Space Telescope Science Institute, which is operated by the Association of Universities for Research in Astronomy, Inc., under NASA contract NAS 5-26555.

RGA thanks NSERC, the Government of Ontario, and the Canada Foundation for Innovation for funding provided by an E. W. R. Steacie Memorial Fellowship. KG & SS acknowledge generous funding from the David and Lucille Packard Foundation. H.-W.C. acknowledges support by NASA through a Hubble Fellowship grant HF-01147.01A from the Space Telescope Science Institute, which is operated by the Association of Universities for Research in Astronomy, Incorporated, under NASA contract NAS5-26555. DLB wishes to thank the Centre National d'Etudes Spatiales for its support.

Appendices

A. ROBUSTNESS OF THE QUASI-PETROSIAN GINI COEFFICIENT AS A GALAXY CLASSIFIER

In this Appendix we will investigate the robustness of our galaxy classification methodology. As described in Section 4, our classifications are based on a galaxy's position in the Asymmetry vs. Gini diagram. For purposes of computing the mass function of early-type galaxies, we have shown in the text that the Gini coefficient plays a much more significant role than does asymmetry. In fact, the main conclusions of this paper would remain unchanged if asymmetry were neglected completely. Therefore our aim in this appendix is to demonstrate that the Gini coefficient measured in a single red band (F814W) can be used as a simple and very robust classifier of early-type galaxy morphology out to $z \sim 2$. We emphasize at the outset that this claim is true *only* when data is deep enough to allow quasi-Petrosian isophotes to be used to calculate the Gini coefficient, as described in the text.

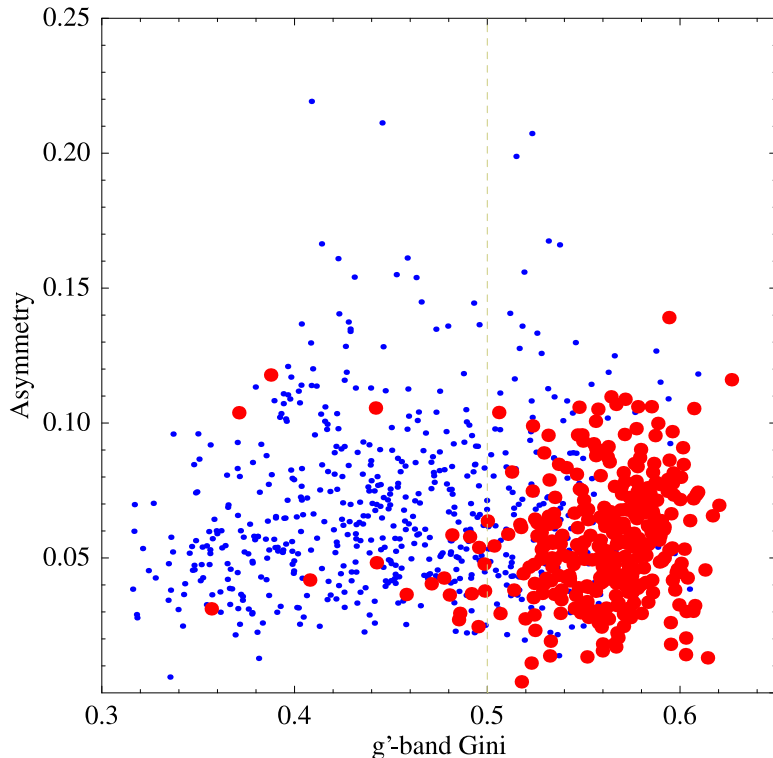


Fig. 12.— Asymmetry vs. Gini coefficient for 800 nearby galaxies observed in g' -band as part of the Sloan Digital Sky Survey. Quasi-Petrosian thresholds were used when measuring both quantities, as described in the text. Galaxies classified visually as being early-type systems are shown in red. The vertical line denotes the $G = 0.5$ cut used to distinguish early-type galaxies from all other systems.

Our analysis of the robustness of the quasi-Petrosian Gini coefficient is based on measurements of this quantity obtained through u' , g' , r' and i' filters for 800 nearby galaxies in the Sloan Digital Sky Survey (SDSS). This is a subset of the morphological sample analyzed by Nair et al. (2007). We refer readers to that paper for additional details. Nair et al. (2007) will also present detailed comparisons of classifications made using quasi-Petrosian Gini coefficients to those made using other methods. Our ACS imaging sample has a signal-to-noise ratio floor of 100 (only a single galaxy in our ACS imaging sample has a signal-to-noise ratio below this) so our analysis will be restricted to galaxies with a u' -band signal-to-noise ratio > 100 .

Figure 12 shows the Asymmetry vs. Gini coefficient diagram for g' -band imaging of our SDSS sample. Galaxies classified visually by one of us (Preethi Nair) as being early-type systems are shown in red. The vertical line denotes the $G = 0.5$ cut used to distinguish early-type galaxies from all other systems. It is seen that this simple bifurcation of the A-G plane into two parts does a rather good job of distinguishing early-type galaxies from all other systems. As expected, there is some leakage of visually-classified early-type galaxies to regions of the diagram with $G < 0.5$, and some leakage in the other direction (non-early-types into the $G > 0.5$). These systems are almost all early-type spirals whose visual classifications are known (based on comparisons of visual classifications between observers, e.g. Nair et al. 1995) to be ambiguous (e.g. Sa vs. S0/a vs. S0 systems).

The $G = 0.5$ cut evidently does a good job of distinguishing high signal-to-noise g' -band images of SDSS early-type galaxies from the rest of the galaxy population, but how robust is this cut to changes in rest wavelength of observation, and to decreasing signal-to-noise? Figure 13 is an attempt to address this question. The top row of Figure 13 shows the Gini coefficients of our SDSS reference sample measured at different wavelengths (using u' , g' , and i' filters) plotted against the Gini coefficients in g' -band. The diagonal line shown in each panel delineates a perfect mapping between the two parameters, *i.e.* no change in Gini as a function of wavelength. The quasi-Petrosian Gini coefficient is seen to be remarkably robust to changes in rest wavelength when measured from data with reasonably high signal-to-noise. The Gini coefficient measured in g' -band barely changes when measured in r' -band and i' -band, and for early-type galaxies in particular the changes are hardly bigger than the random measurement errors (Nair et al. 2007). Measurements of the u' -band Gini coefficient probe wavelengths blueward of the 4000Å break, and our naïve expectation was that Gini coefficients *should* be significantly different in u' -band when compared with measurements made at wavelengths redward of the break. At first inspection Figure 13 does seem to show this, in the form of systematic offsets between the g' -band and u' -band images. However, a more careful inspection shows that the trends seen are almost certainly due to the the low signal-to-noise ratio of the u' -band data, instead of being due to systematic differences in the intrinsic g' -band and u' -band images of galaxies.

Each panel in Figure 13 records the mean signal-to-noise level of the sample being plotted. It is seen that the SDSS u' -band data has a mean signal-to-noise ratio of ~ 130 , which is a factor two to three lower than the mean signal-to-noise ratios of our ACS images, and about a factor of five lower than the signal-to-noise ratios of the corresponding SDSS g' , r' , and i' images. It is clear that these differing signal-to-noise ratios need to be accounted for before comparing the u' -band Gini coefficients of the data obtained at different wavelengths. This is a crucial point, because the ACS F814W filter begins to probe blueward of the 4000Å break at $z > 1$, where the bulk of our data lies. Since the SDSS u' -band filter data would seem to provide the best match to the rest-frame wavelengths being probed by much of our ACS data, understanding the reason why the Gini coefficients of u' -band data shown in Figure 13 appear be systematically lower than those measured at longer wavelengths is of special significance. The columnar base of the ‘T’ in Figure 13 is an attempt to understand the u' -band data by showing how the Gini coefficient of g' -band sample changes when noise is added to the images to lower the mean signal-to-noise ratios of the samples plotted. The mean signal-to-noise ratio of the noise-degraded g' -band data in middle panel is similar to the mean signal-to-noise ratio for galaxies at $z > 1.2$ in our sample. The mean signal-to-noise ratio of the lowest panel is similar to that of the data in the SDSS u' -band sample. The strong resemblance between this panel and the u' -band panel at the top left of the Figure suggests that the apparent offset in the Gini coefficients of the high signal-to-noise g' -band data and the low signal-to-noise u' -band data is mostly due to poor signal in the latter, and not due to morphological K-corrections.

A more explicit comparison of u' -band and noise-degraded g' -band Gini coefficients of our local calibration sample is shown in Figure 14. The mean signal-to-noise ratio of the g' -band sample has been harmonized to be nearly identical that that of the u' -band sample. Within the scatter introduced by random measurement error, Gini coefficient measurements at g' -band and u' -band are identical, even though these bands straddle the 4000Å break (at which point visual morphologies of galaxies can appear to make large changes). This highlights the strongest benefit of using an abstract quantity like the quasi-Petrosian Gini coefficient as measure of morphology. This is also the essence of our contention, made repeatedly in the main text of this paper, that if quasi-Petrosian Gini coefficients are used to quantify morphology, then a basic ‘cure’ for the deleterious effects of morphological K -corrections is simply to obtain deeper data.

We conclude this appendix with Figure 15, which shows an object-by-object postage-stamp image montage of galaxies near the $G = 0.5$ border of the Gini coefficient vs. redshift diagram. This diagram can be used to inspect

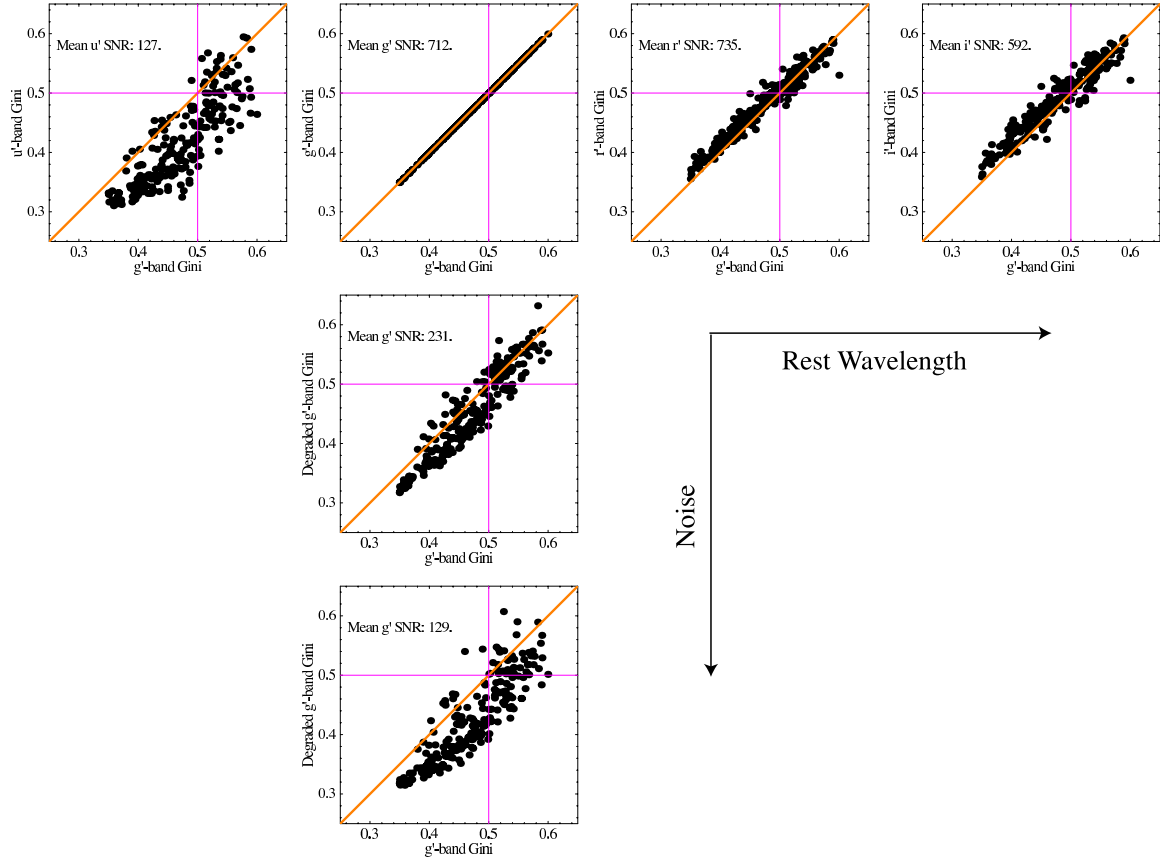


Fig. 13.— Analysis of the robustness of the quasi-Petrosian Gini coefficient, based on measurements of this quantity obtained through u' , g' , r' and i' filters for 800 nearby galaxies in the Sloan Digital Sky Survey (SDSS). The x-axis of each panel in this figure is keyed to the g' -band Gini coefficient measured for each galaxy in this sample. The top row shows the Gini coefficients obtained at different wavelengths (through u' , g' , and i' filters) plotted against the Gini coefficients in g' -band. The diagonal line shown in each panel has a slope of unity and intersects the origin, and therefore corresponds to no change in Gini as a function of wavelength. Vertical and horizontal lines shown in each panel at Gini coefficients of 0.5 correspond to our proposed cutoff for early and late-type galaxies. Changes in the Gini coefficient are remarkably small over the entire wavelength range spanning the g' through i' filter set. While Gini seems to change significantly when comparing u' -band to i' -band in the SDSS, this is easily shown to be an artifact introduced by the low signal-to-noise in the SDSS u' -band data (which is typically much shallower than that obtained in other bands). To explore the sensitivity of the Gini coefficient to noise, the base of the ‘T’ in the figure shows how the Gini coefficient of g' -band sample changes when noise is added to the images. The mean signal-to-noise ratio of the noise-degraded g' -band data in middle panel is similar to the mean signal-to-noise ratio for galaxies at $z > 1.2$ in our sample. The mean signal-to-noise of the bottom panel is similar to that of galaxies with the poorest data in our high-redshift sample, and also to the mean signal-to-noise of the data in the SDSS u' -band sample. The Gini coefficients of noise-degraded g' -images and u' -band images are compared explicitly in the next figure.

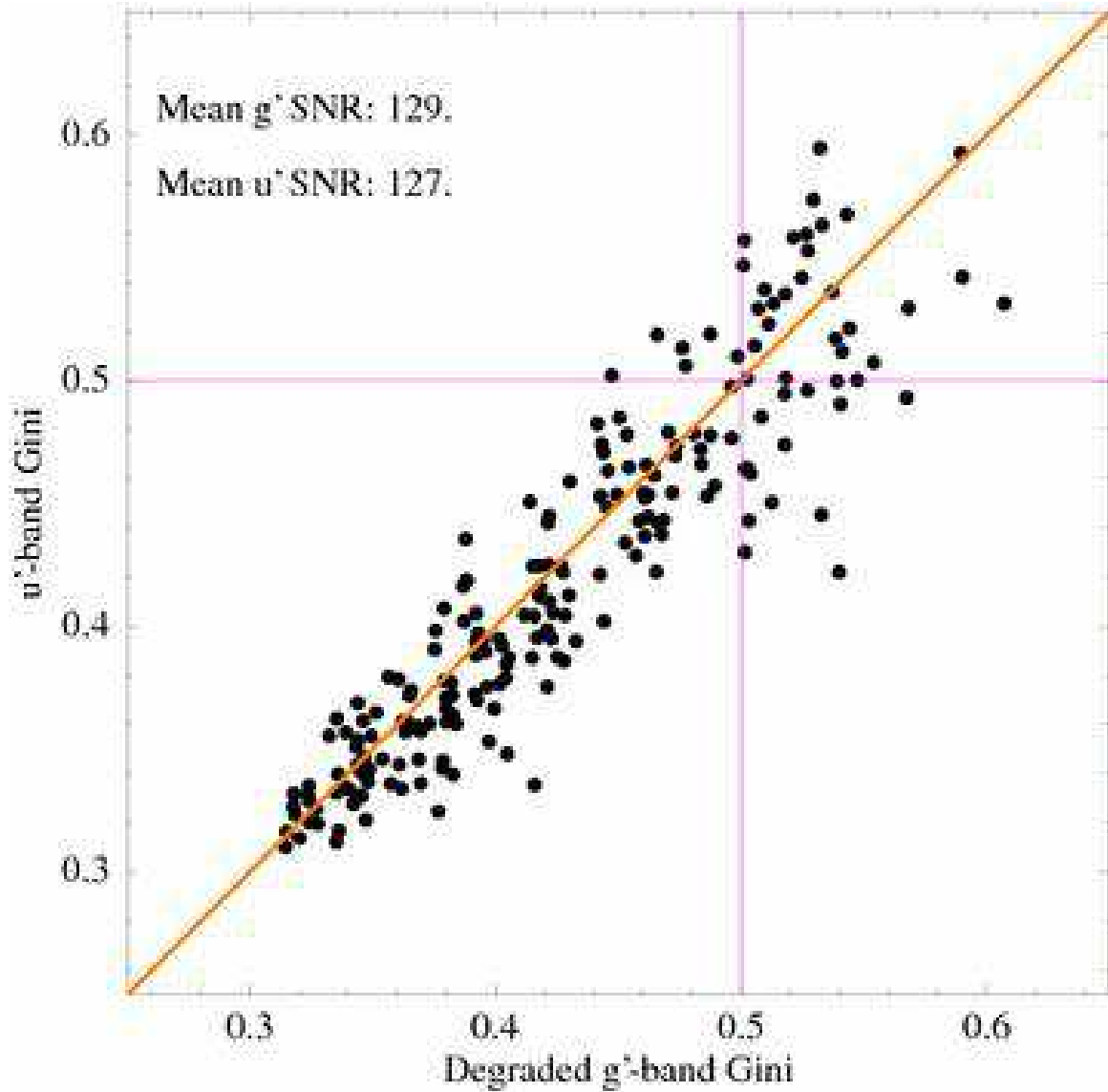


Fig. 14.— Gini coefficients of u' -band galaxies in the SDSS compared to Gini coefficients of corresponding noise-degraded g' -band images. The mean signal-to-noise ratios of the samples have been harmonized to be nearly identical (~ 130). The scatter is consistent with the random measurement error at these low signal-to-noise levels (see Nair et al. 2007 for details). As described in the text, when a quasi-Petrosian formalism is adopted for making the measurements, an individual galaxy's Gini coefficient is nearly independent of its wavelength of observation.

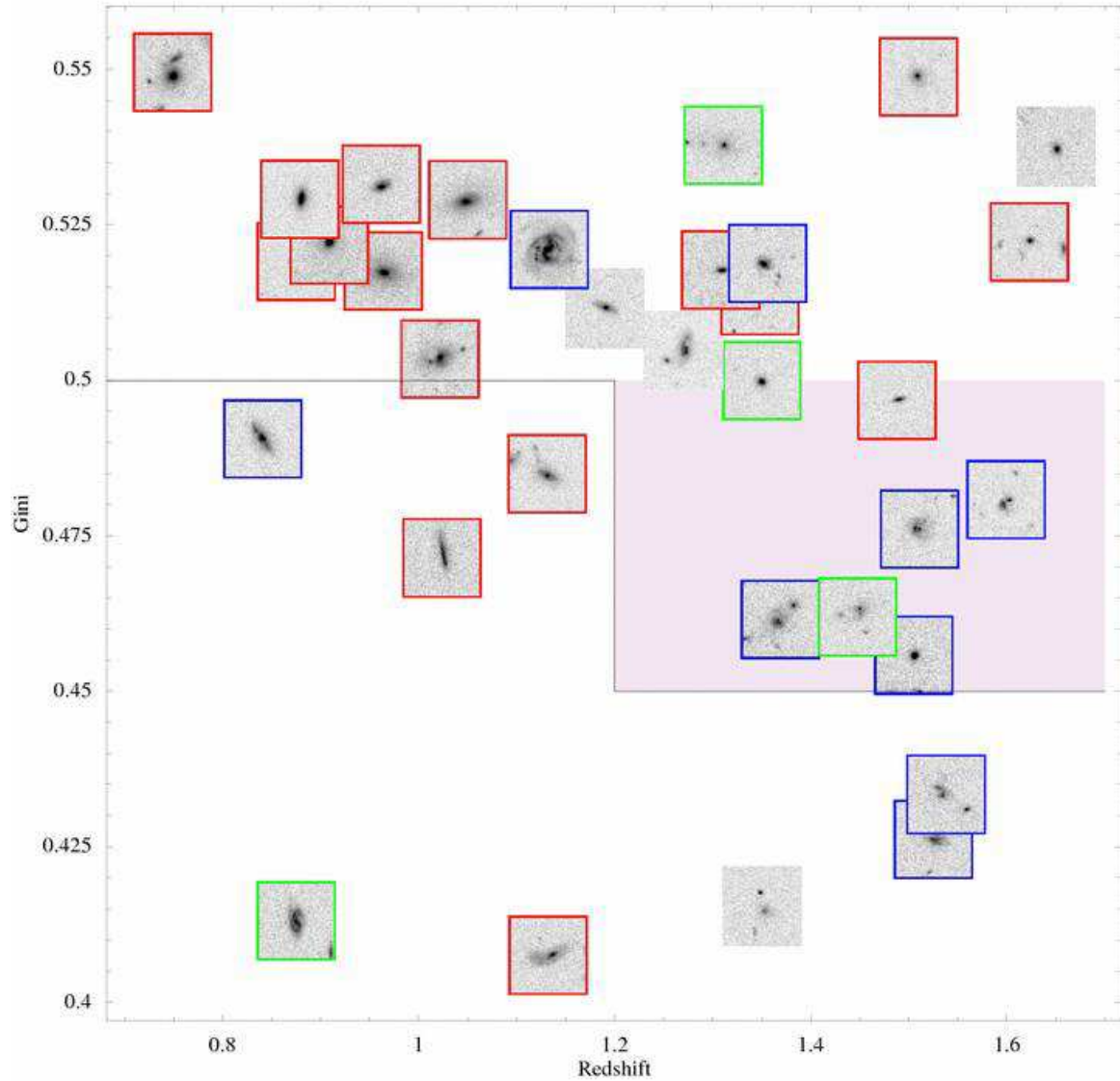


Fig. 15.— An object-by-object comparison of Gini coefficient vs. redshift for galaxies near the border of the $G = 0.5$ cutoff threshold used to discriminate between early-type galaxies and all other systems. Objects in the gray region shown are worth looking at individually because they are at redshifts where F814W imaging is probing blueward of the 4000Å break and also because they are near enough to the $G = 0.5$ cutoff that they could be brought below it at very low signal-to-noise. However, all these objects are seen to be high signal-to-noise systems, and only one object has a visual morphology even remotely consistent with that of an early-type galaxy. As in Fig. 5, the border of each postage stamp is colored according to its spectral classification based on the system described in Paper I. See caption to Fig. 5 for details.

the morphologies of objects near the cutoff threshold used to discriminate between early-type galaxies and all other systems in the present paper. Objects in the gray region shown in Figure 15 shown are of particular interest, because these systems are at redshifts where F814W imaging is probing blueward of the 4000Å break, and also near enough to the $G = 0.5$ cutoff that they could conceivably be brought below it at very low signal-to-noise. However, all these objects are seen to be high signal-to-noise systems, and only one object (with a high star-formation rate spectrum) has a visual morphology even remotely consistent with that of an early-type galaxy.

REFERENCES

Abraham, R. G., van den Bergh, S., Glazebrook, K., Ellis, R. S., Santiago, B. X., Surma, P., & Griffiths, R. E. 1996, *ApJS*, 107, 1

Abraham, R. G., Ellis, R. S., Fabian, A. C., Tanvir, N. R., & Glazebrook, K. 1999, *MNRAS*, 303, 641

Abraham, R. G., van den Bergh, S., & Nair, P. 2003, *ApJ*, 588, 218

Abraham, R. G., et al. 2004, *AJ*, 127, 2455

Baldry, I. K., & Glazebrook, K. 2003, *ApJ*, 593, 258

Baugh, C. M., Cole, S., & Frenk, C. S. 1996, *MNRAS*, 283, 1361

Bauer, A. E., Drory, N., Hill, G. J., & Feulner, G. 2005, *ApJ*, 621, L89

Bell, E. F., McIntosh, D. H., Katz, N., & Weinberg, M. D. 2003, *ApJS*, 149, 289

Bell, E. F., et al. 2004, *ApJ*, 608, 752

Bertin, E., & Arnouts, S. 1996, *A&AS*, 117, 393

Blanton, M. R., et al. 2001, *AJ*, 121, 2358

Borch, A., et al. 2006, *A&A*, 453, 869

Bouwens, R. J., et al. 2005, *ApJ*, 624, L5

Brinchmann, J., et al. 1998, *ApJ*, 499, 112

Brinchmann, J., & Ellis, R. S. 2000, *ApJ*, 536, L77

Bundy, K., et al. 2006, *ApJ*, 651, 120

Chen, H.-W., et al. 2002, *ApJ*, 570, 54

Cimatti, A., et al. 2002, *A&A*, 381, L68

Cimatti, A., et al. 2004, *Nature*, 430, 184

Conselice, et al. 2005, *ApJ*, 620, 564

Coe, D., Benítez, N., Sánchez, S. F., Jee, M., Bouwens, R., & Ford, H. 2006, *AJ*, 132, 926

Conselice, C. J. 2003, *ApJS*, 147, 1

Cowie, L. L., Songaila, A., Hu, E. M., & Cohen, J. G. 1996, *AJ*, 112, 839

Croton, D. J., et al. 2006, *MNRAS*, 365, 11

De Lucia, G., Kauffmann, G., Springel, V., White, S. D. M., Lanzoni, B., Stoehr, F., Tormen, G., & Yoshida, N. 2004, *MNRAS*, 348, 333

Dickinson, M., Papovich, C., Ferguson, H. C., & Budavári, T. 2003, *ApJ*, 587, 25

Faber, S. M., et al. 2005, ArXiv Astrophysics e-prints, arXiv:astro-ph/0506044

Fioc, M. & Rocca-Volmerange, B. 1997, *A&A*, 326, 950

Fontana, A., et al. 2004, *A&A*, 424, 23

Fontana, A., et al. 2006, *A&A*, 459, 745

Ford, H. C., et al. 2003, *Proc. SPIE*, 4854, 81

Giavalisco, M., et al. 2004, *ApJ*, 600, L103

Gini, C. 1912. Reprinted in Memorie di metodologia statistica (Ed. E.Pizetti and T.Salvemini.) Rome: Libreria Eredi Virgilio Veschi, 1955.

Glazebrook, K., & Bland-Hawthorn, J. 2001, *PASP*, 113, 197

Glazebrook, K., et al. 2004, *Nature*, 430, 181

Governato, F., Willman, B., Mayer, L., Brooks, A., Stinson, G., Valenzuela, O., Wadsley, J., & Quinn, T. 2006, *MNRAS*, 1424

Heavens, A., Panter, B., Jimenez, R., & Dunlop, J. 2004, *Nature*, 428, 625

Iye et al. 2007, *Nature*, 443, 186

Jimenez, R., Bernardi, M., Haiman, Z., Panter, B., & Heavens, A. F. 2006, ArXiv Astrophysics e-prints, arXiv:astro-ph/0610724

Juneau, S., et al. 2005, *ApJ*, 619, L135

Kauffmann, G., et al. 2003, *MNRAS*, 341, 33

Kauffmann, G., & Charlot, S. 1998, *MNRAS*, 294, 705

Kodama, T., et al. 2004, *MNRAS*, 350, 1005

Kajisawa & Yamada, 2005, *ApJ*, 618, 91

Labbé, I., et al. 2003, *ApJ*, 591, L95

Le Borgne, D., Rocca-Volmerange, B., Prugniel, P., Lançon, A., Fioc, M., & Soubiran, C. 2004, *A&A*, 425, 881

Le Borgne, D., et al. 2006, *ApJ*, 642, 48

Lilly, S. J., Tresse, L., Hammer, F., Crampton, D., & Le Fevre, O. 1995, *ApJ*, 455, 108

Lisker, T., Debattista, V. P., Ferreras, I., & Erwin, P. 2006, *MNRAS*, 370, 477

Lotz, J. M., Primack, J., & Madau, P. 2004, *AJ*, 128, 163

Lotz, J. M., Madau, P., Giavalisco, M., Primack, J., & Ferguson, H. C. 2006, *ApJ*, 636, 592

Mandelbaum, R., Seljak, U., Kauffmann, G., Hirata, C. M., & Brinkmann, J. 2006, *MNRAS*, 368, 715

Menanteau, F., et al. 2004, *ApJ*, 612, 202

McCarthy, P. J., et al. 2001, *ApJ*, 560, L131

McCarthy, P. J., et al. 2004, *ApJ*, 614, L9

Moustakas, L. A., et al. 2004, *ApJ*, 600, L131

Nakamura, O., Fukugita, M., Yasuda, N., Loveday, J., Brinkmann, J., Schneider, D. P., Shimasaku, K., & SubbaRao, M. 2003, *AJ*, 125, 1682

Noll, S., Pierini, D., Pannella, M., & Savaglio, S. 2006, ArXiv Astrophysics e-prints, arXiv:astro-ph/0612080

Papovich, C., Dickinson, M., Giavalisco, M., Conselice, C. J., & Ferguson, H. C. 2005, *ApJ*, 631, 101

Papovich, C., et al. 2006, *ApJ*, 640, 92

Petrosian, V. 1976, *ApJ*, 209, L1

Ravindranath, S., et al. 2006, *ApJ*, 652, 963

Rix, H.-W., et al. 2004, *ApJS*, 152, 163

Savaglio, S., et al. 2005, *ApJ*, 635, 260

Scarlata, C., et al. 2006, ArXiv Astrophysics e-prints, arXiv:astro-ph/0611644

Scoville, N., et al. 2006, ArXiv Astrophysics e-prints, arXiv:astro-ph/0612384

Scoville, N., et al. 2006, ArXiv Astrophysics e-prints, arXiv:astro-ph/0612306

Springel, V., et al. 2005, *Nature*, 435, 629

Steidel et al. 1999, *ApJ*, 519, 1

Steidel, C. C., Adelberger, K. L., Shapley, A. E., Pettini, M., Dickinson, M., & Giavalisco, M. 2003, *ApJ*, 592, 728

Stockton, A., Canalizo, G., & Maihara, T. 2004, *ApJ*, 605, 37

Tremonti, C. A., et al. 2004, *ApJ*, 613, 898

van Dokkum, P. G. 2005, *AJ*, 130, 2647

Wolf, C., et al. 2004, *A&A*, 421, 913

Yan, L., & Thompson, D. 2003, *ApJ*, 586, 765

Yan, H., & Windhorst, R. A. 2004, *ApJ*, 612, L93